PNAS RESEARCH ARTICLE | GENETICS

Dual modes of DNA N^6-methyladenine maintenance by distinct methyltransferase complexes

Yuanyuan Wang[a,b,1,2], Bei Nan[a,b,1], Fei Ye[a,b,1], Zhe Zhang[a,b,1], Wentao Yang[c,1], Bo Pan[a,b], Fan Wei[a,b], Lili Duan[a,b], Haicheng Li[a,b], Junhua Niu[a,b], Aili Ju[a,b], Yongqiang Liu[a,b], Dantong Wang[d], Wenxin Zhang[e], Yifan Liu[c,2], and Shan Gao[a,b,2]

Edited by Sigrid Nachtergaele, Yale University, New Haven, CT; received July 1, 2024; accepted December 2, 2024 by Editorial Board Member John R. Carlson

Stable inheritance of DNA N^6-methyladenine (6mA) is crucial for its biological functions in eukaryotes. Here, we identify two distinct methyltransferase (MTase) complexes, both sharing the catalytic subunit AMT1, but featuring AMT6 and AMT7 as their unique components, respectively. While the two complexes are jointly responsible for 6mA maintenance methylation, they exhibit distinct enzymology, DNA/chromatin affinity, genomic distribution, and knockout phenotypes. AMT7 complex, featuring high MTase activity and processivity, is connected to transcription-associated epigenetic marks, including H2A.Z and H3K4me3, and is required for the bulk of maintenance methylation. In contrast, AMT6 complex, with reduced activity and processivity, is recruited by PCNA to initiate maintenance methylation immediately after DNA replication. These two complexes coordinate in maintenance methylation. By integrating signals from both replication and transcription, this mechanism ensures the faithful and efficient transmission of 6mA as an epigenetic mark in eukaryotes.

DNA N^6-methyladenine (6mA) | maintenance methylation | methyltransferase | AMT1 | PCNA

DNA N^6-methyladenine (6mA) is well documented in prokaryotes, serving crucial functions in maintaining genome integrity and regulating replication and transcription (1). Recent studies have unveiled its pervasive presence in eukaryotes, albeit with notable variation in abundance and functionality across species (2–5). In animals, plants, and higher fungi, 6mA is sparse, distributed with no specific sequence context, and frequently associated with transcriptionally inactive regions, raising questions over whether it serves as an enzymatically deposited epigenetic mark (6–15). By contrast, in protists, green algae, and basal fungi, 6mA is abundant, present preferentially, if not exclusively, at the ApT dinucleotide, and associated with RNA polymerase II (Pol II)-transcribed genes, supporting its role as an epigenetic mark (3–5, 16–18).

As an epigenetic mark, 6mA must be stably propagated. The inheritance mechanism of 6mA is a crucial aspect of 6mA biology in eukaryotes. We and others have recently established 6mA as an enzymatically deposited and heritable epigenetic modification in the unicellular eukaryote *Tetrahymena thermophila* (3, 16, 17, 19). 6mA is faithfully transmitted through a semiconservative mechanism dependent on an MT-A70 family member, AMT1 (adenine methyltransferase 1) (19). It is enriched toward the 5′ end of the gene body (3) and on linker DNA flanked by nucleosomes decorated with the histone variant H2A.Z and the histone modification H3 lysine 4 trimethylation (H3K4me3) (17). Reduced 6mA level alters gene expression, diminishes growth, and generates defects in morphology and behavior (17). However, how this stereotypical 6mA distribution pattern is faithfully and efficiently transmitted remains unclear. The connection of 6mA with other epigenetic marks, and the coordination between the methylation process on the one hand, and DNA replication and transcription on the other, still need to be explored.

Here, we characterize two AMT1-containing methyltransferase (MTase) complexes, distinguished by the inclusion of two mutually exclusive components, AMT6 and AMT7. AMT7 complex exhibits high MTase activity and processivity, with its distribution strongly correlated with transcription-associated epigenetic marks, especially H2A.Z and H3K4me3. It is recruited by these epigenetic pathways and required for most of maintenance methylation. In contrast, AMT6 complex exhibits reduced MTase activity and processivity, and is more widely distributed. It is recruited by PCNA to facilitate the initiation of maintenance methylation after DNA replication. This dual-mode system achieves precise and rapid methylation through multiple recognitions, integrates signals from both replication and transcription, and ensures transmission of 6mA as an epigenetic mark.

Significance

DNA N^6-methyladenine (6mA) has recently been recognized as an epigenetic mark in eukaryotes. The stable inheritance of 6mA is essential for its biological functions. However, the precise mechanisms by which 6mA patterns are faithfully and efficiently transmitted remain largely unknown. Here, we have identified two distinct 6mA methyltransferase complexes and elucidated their coordinated role in maintenance methylation. This dual-complex mechanism ensures rapid and accurate methylation at newly replicated loci with proper transcription-associated epigenetic marks.

Author affiliations: [a]Key Laboratory of Evolution & Marine Biodiversity (Ministry of Education) and Institute of Evolution & Marine Biodiversity, Ocean University of China, Qingdao 266003, China; [b]Laboratory for Marine Biology and Biotechnology, Qingdao Marine Science and Technology Center, Qingdao 266237, China; [c]Department of Biochemistry & Molecular Medicine, University of Southern California Keck School of Medicine, Los Angeles, CA 90033; [d]BGI Research, Qingdao 266555, China; and [e]Institute of Biomedical Research, Yunnan University, Kunming 650500, China

Author contributions: Y.W., Yifan Liu, and S.G. designed research; Y.W., B.N., Z.Z., F.W., L.D., J.N., A.J., and Yongqiang Liu performed research; F.Y., W.Y., B.P., H.L., D.W., and W.Z. analyzed data; and Y.W., Yifan Liu, and S.G. wrote the paper, with inputs from all authors.

The authors declare no competing interest.

This article is a PNAS Direct Submission. S.N. is a guest editor invited by the Editorial Board.

[1]Y.W., B.N., F.Y., Z.Z., and W.Y. contributed equally to this work.

[2]To whom correspondence may be addressed. Email: wangyuanyuan@ouc.edu.cn, Yifan.Liu@med.usc.edu, or shangao@ouc.edu.cn.

This article contains supporting information online at https://www.pnas.org/lookup/suppl/doi:10.1073/pnas.2413037121/-/DCSupplemental.

Published January 15, 2025.

Results

Two Distinct AMT1 Complexes with AMT6 or AMT7 as Their Mutually Exclusive Components. We performed immunoprecipitation and mass spectrometry (IP-MS) using AMT1 as bait (*SI Appendix*, Fig. S1*A* and Table S1). In addition to the previously reported interacting proteins, namely AMT7, AMTP1, and AMTP2 (referred to as MTA9, p1, and p2 in ref. 16), we also identified AMT6 (referred to as MTA9-B in ref. 16), another MT-A70 family member (Fig. 1*A* and *SI Appendix*, Table S2). We then performed reciprocal IP with AMT6 and AMT7 as bait. MS revealed that both AMT6 and AMT7 interacted with AMT1, AMTP1, and AMTP2 (Fig. 1*A* and *SI Appendix*, Table S3). These interactions were corroborated by immunoblotting (Fig. 1*B*). Importantly, in AMT7 IP, we could not detect AMT6, and vice versa (Fig. 1 *A* and *C* and *SI Appendix*, Table S3). Therefore, even though AMT6 and AMT7 share their core interactomes, they form two distinct and mutually exclusive complexes: AMT6-AMT1-AMTP1-AMTP2 (hereafter referred to as AMT6 complex) and AMT7-AMT1-AMTP1-AMTP2 (AMT7 complex) (Fig. 1*D*).

AMT7 complex corresponds to the originally identified and characterized AMT1 complex (16, 19). However, AMT6 has been reported to fractionate separately from AMT1 (16), thus requiring further scrutiny. *AMT6* expression was elevated during vegetative growth (asexual reproduction) and conjugation (sexual reproduction), but diminished during starvation (cell cycle arrest), in a pattern very similar to that of AMT7, as well as AMT1, AMTP1, and AMTP2 (*SI Appendix*, Fig. S1*B*). Like AMT1 and AMT7, AMT6 was also localized in the transcriptionally active macronucleus (MAC) but not in the transcriptionally inert micronucleus

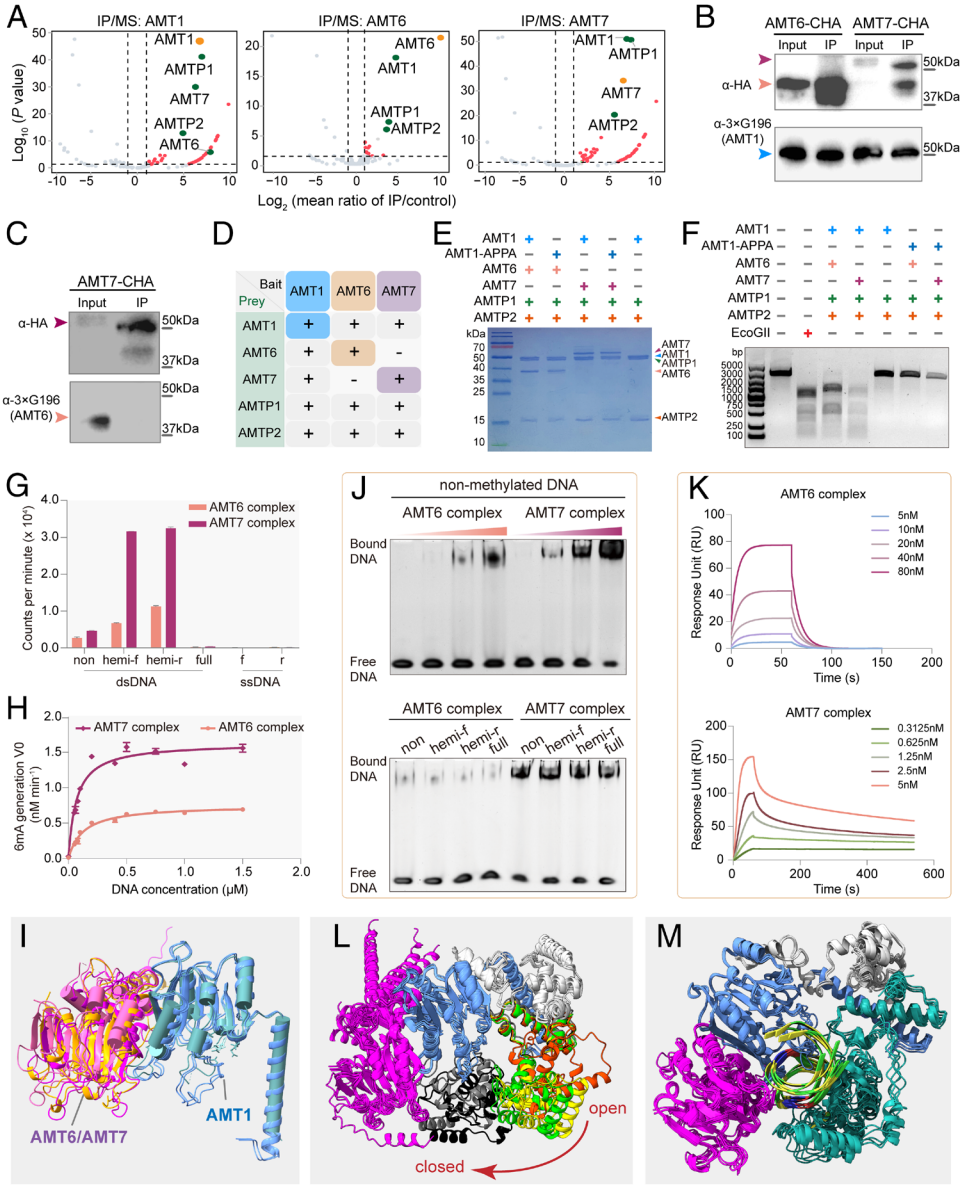

Fig. 1. Two distinct AMT1 complexes with AMT6 or AMT7 as their mutually exclusive components. (*A*) Volcano plots of IP-MS results using AMT1, AMT6, and AMT7 as the bait. Bait: orange; high-confidence preys of interest: green; other high-confidence preys: red; low-confidence preys: gray. (*B*) IP-IB confirming the interaction of AMT1 with AMT6 and AMT7, respectively. Bait proteins were tagged with a hemagglutinin (HA), while prey proteins were tagged with 3×G196. (*C*) IP-IB confirming the lack of interaction between AMT6 and AMT7. Bait proteins were HA-tagged, while prey proteins were tagged with 3×G196. (*D*) Summary of interactions between AMT1 complexes according to IP-MS results. (*E*) SDS-PAGE analysis of recombinant AMT6 and AMT7 complexes with bacterially expressed proteins. (*F*) Detection of DNA methyltransferase (MTase) activities by *Dpn*I digestion. Linearized plasmid DNA purified from *dam*⁻ *Escherichia coli* was subject to in vitro methylation. Only methylated DNA was digested by *Dpn*I, as seen in lanes treated by wild-type (WT) AMT6 and AMT7 complexes, as well as EcoGII. (*G*) Detection of DNA MTase activities by [^{3}H]SAM labeling. 27bp double-strand DNA (dsDNA) substrates, with two ApT dinucleotides in the nonmethylated state (non), hemimethylated on the forward strand (hemi-f), hemimethylated on the reverse strand (hemi-r), or fully methylated (full), were subject to in vitro methylation by AMT6 and AMT7 complexes. DNA methylation was monitored by scintillation counting. Only background methylation was observed in fully methylated dsDNA, or single-strand DNA (ssDNA: f/r). Error bars represent SD (n = 3). (*H*) Enzyme kinetics of AMT6 and AMT7 complexes on hemimethylated DNA, quantified by [^{3}H]SAM-labeling. Each data point was presented as mean ± SD (n = 3). Curve fitting was based on steady-state Michaelis–Menten kinetics. (*I*) Comparing AF3-predicted and published cryo-EM structures (20) of the heterodimeric core of AMT1 complexes. For AF3 modeling: AMT1, blue; AMT6, orange; AMT7, magenta. For the cryo-EM structure of AMT7 complex: AMT1, cadet blue; AMT7, hot pink; displayed as tube helices. (*J*) Detection of DNA binding by Electrophoretic Mobility Shift Assay (EMSA). *Top* panel: bound DNA (top band) progressively increased, while free DNA (Bottom) progressively decreased, as AMT6 and AMT7 complexes increased in concentration (1, 2, 4, 8 μM protein, 4 μM DNA); DNA binding ability was more prominent for AMT7 complex than AMT6 complex. 27bp nonmethylated DNA was used as substrate. *Bottom* panel: no substantial difference between dsDNA of different methylation states. (*K*) Detection of DNA binding by Surface Plasmon Resonance (SPR). Hemimethylated dsDNA was immobilized, while specified concentrations of AMT6 and AMT7 complexes were flowed. Equilibrium and kinetic constants were calculated by fitting to 1:1 Langmuir binding model. (*L*) AF3 predictions of the AMT7 apo-complex. Five high-confidence structures were used to illustrate the open to closed transition: AMT1, cornflower blue; AMT7, magenta; AMTP2, light gray; AMTP1, from open to closed: red, yellow, green, gray, and dark gray. (*M*) AF3 predictions of the AMT7 holo-complex bound to a dsDNA substrate (depicted in the double helix form). Five high-confidence structures were used to depict the stable conformations, with AMT1 in cornflower blue, AMT7 in magenta, AMTP2 in light gray, and AMTP1 in light sea green.

(MIC) during vegetative growth, as shown by immunofluorescence (IF) staining (*SI Appendix*, Fig. S1*C*). During conjugation, AMT6 was detected in the parental MAC at prezygotic stages and then in the new MAC at postzygotic stages (*SI Appendix*, Fig. S1*D*). This localization pattern is consistent with that of 6mA (17, 21), supporting AMT6's role in 6mA transmission.

Phylogenetic analysis grouped AMT6 and AMT7 in the same clade of the MT-A70 family, separate from the AMT1 clade (*SI Appendix*, Fig. S1*E*) (17). Both AMT6 and AMT7 lacked the conserved MTase signature motif ([DNSH]PP[YFW]) required for catalytic activity (NIKW in AMT6 and NALW in AMT7) (*SI Appendix*, Fig. S1 *F* and *G*) (22), which is present in AMT1 (DPPW). AMT6 and AMT7 homologs were found in a wide range of unicellular eukaryotes, but absent in multicellular eukaryotes, mirroring the phylogenetic distribution of AMT1 (*SI Appendix*, Fig. S1*H*) (17).

Differential Activities of Reconstituted AMT6 and AMT7 Complexes. We next reconstituted AMT6 and AMT7 complexes with bacterially expressed proteins (Fig. 1*E*). Their components cofractionated during size exclusion chromatography (*SI Appendix*, Fig. S1*I*), consistent with two stable complexes. Both complexes showed robust MTase activities, assayed by *Dpn*I digestion of methylated plasmid DNA (Fig. 1*F*) or scintillator count after ^{3}H-SAM labeling of short double-stranded DNA (dsDNA) (Fig. 1*G*). For both complexes, we also observed higher MTase activities on the hemimethylated substrate compared to the nonmethylated substrate (Fig. 1*G*), in line with their role in maintenance methylation (19). No activity was observed for single-stranded DNA (ssDNA) (Fig. 1*G*). The MTase activity for AMT7 complex was substantially higher than AMT6 complex, as quantified by the steady-state kinetics using the hemimethylated short dsDNA substrate (AMT7: K_m = 0.069 μM, k_{cat} = 0.033 min^{-1}; AMT6: K_m = 0.126 μM, k_{cat} = 0.015 min^{-1}) (Fig. 1*H*).

Notably, AMT1, AMTP1, and AMTP2 formed a stable subcomplex (hereafter referred to as AMT1 subcomplex; Fig. 1*E*). However, in the absence of AMT6 and AMT7, it did not have any MTase activity; neither did an AMT7 complex with AMT1 mutated at the MTase signature motif (DPPW to APPA) (Fig. 1*F*). Therefore, even though AMT1 subcomplex contains the catalytically critical subunit, it only becomes active after forming a full complex by incorporating either AMT6 or AMT7. Using AlphaFold 3 (AF3), we performed structure modeling of AMT6 and AMT7 apo-complexes (without DNA substrate) (Fig. 1*I*). At the AMT1-AMT7 heterodimeric core, AF3-predicted structures of AMT7 apo-complex were essentially identical to that solved by cryoelectron microscopy (Fig. 1*I*; rmsd = 1.8 Å) (20). The AF3-predicted AMT1-AMT6 interface was very similar to the AMT1-AMT7 interface (Fig. 1*I*, rmsd = 1.36 Å; surface area buried: 2,166 vs. 2,274 $Å^2$), with many shared interface residues (*SI Appendix*, Fig. S1*J*).

AMT6 and AMT7 complexes specifically bound dsDNA (*SI Appendix*, Fig. S1*K*), regardless of its methylation state (Fig. 1 *J*, *Bottom*). AMT7 complex showed a much higher DNA binding affinity than AMT6 complex, as revealed by SPR (Fig. 1*K*) and EMSA (Fig. 1*J*). The disassociation constant (K_D), as quantified by SPR, was much lower for AMT7 complex ($K_D = 2.315 \times 10^{-10}$M; $k_a = 6.688 \times 10^6$/Ms and $k_d = 1.548 \times 10^{-3}$/s) than for AMT6 complex ($K_D = 6.498 \times 10^{-6}$M; $k_a = 3.894 \times 10^4$/Ms and k_d = 0.2531/s) (Fig. 1*K*). Notably, EMSA showed that AMT1 subcomplex had low DNA binding affinity (*SI Appendix*, Fig. S1*L*). Also, AMT7 alone did not bind DNA as tightly as AMT7 complex (*SI Appendix*, Fig. S1*M*).

Recent structural analyses of AMT7 apo-complex have revealed the AMT1-AMT7 heterodimeric core and its extension comprising the N-terminal helix of AMT1, AMTP2, and the helix–turn–helix-like domain of AMTP1 (20, 23). However, the DNA-binding domain (DBD) of AMTP1, long proposed to play a role in binding of the dsDNA substrate (16, 20), is not resolved in the apo-complex (20, 23). To shed light on the structural basis of DNA binding, we performed structure modeling by AF3. We observed that in AMT7 apo-complex, AMTP1 DBD had a well-defined local structure, but its global position varied greatly, most likely reflecting the structural flexibility of the loop region connecting AMTP1 DBD to the rest of the complex (Fig. 1*L*, *SI Appendix*, Fig. S1*N*, and Movie S1). Most predictions placed DBD far away from AMT7, representing various open forms of AMT7 complex. Only occasionally was DBD found near AMT7. Physical proximity of AMTP1 DBD and AMT7, while only present dynamically, was captured by crosslinking mass spectrometry (*SI Appendix*, Fig. S1*O*). Intriguingly, for AMT7 holo-complex (with DNA substrate), DBD was well defined both locally and globally in structure modeling (Fig. 1*M*). Indeed, DBD was only found at a specific position very close to AMT7, while engaging the dsDNA substrate in the major groove. Similar results were obtained for AMT6 apo-complex and holo-complex (*SI Appendix*, Fig. S1 *P–R* and Movie S2). These observations strongly suggest that DNA binding drives AMT6/AMT7 complex from various open forms to a single closed form, with a clamp-like structure comprising AMT6/AMT7, AMT1, and AMTP1 wrapped around dsDNA. Building on these insights, we postulate that maintenance methylation by AMT6/AMT7 complex involves multiple steps, starting from the competitive assembly of the apo-complex and culminating in the establishment of the closed-form holo-complex.

Divergent Phenotypes of Δ*AMT6* and Δ*AMT7*. Having identified AMT6 and AMT7 complexes and characterized their differential activities, we performed loss-of-function genetic studies of AMT6 and AMT7. Δ*AMT7* largely phenocopied Δ*AMT1* (17): along with substantial global reduction of 6mA, as quantified by IF and MS (*SI Appendix*, Fig. S2 *A* and *B*), these mutants grew much more slowly than WT (2.6× WT doubling time) (*SI Appendix*, Fig. S2*C*); many cells contained a dysfunctional contractile vacuole (Fig. 2*A*). In contrast, Δ*AMT6* behaved more like WT, with global 6mA level, growth rate, and contractile vacuole barely affected (Fig. 2*A* and *SI Appendix*, Fig. S2 *A–C*).

We used Single Molecule, Real-Time (SMRT) sequencing in the Circular Consensus Sequences (CCS) mode (also referred to as PacBio HiFi sequencing) to analyze 6mA distribution in *Tetrahymena* genomic DNA, which was corroborated by 6mA-IP sequencing (*SI Appendix*, Fig. S2 *D–G*). 1,259,892 and 730,284 high-quality reads (corresponding to 31× and 27× coverage of the *Tetrahymena* MAC genome, respectively) were obtained from native genomic DNA samples of vegetatively growing Δ*AMT6* and Δ*AMT7* cells (*SI Appendix*, Table S4). Essentially all 6mA occurred on the ApT dinucleotide (6mApT) (*SI Appendix*, Fig. S2 *H–J*) (19). This specific sequence context also argues against random incorporation of salvaged 6mA during DNA synthesis, as is likely the case in many metazoan systems lacking enzymatically deposited 6mA (24). Indeed, non-ApT 6mA levels in native genomic DNA were as low as those in whole-genome amplification samples used as the negative control (*SI Appendix*, Fig. S2*K*). Furthermore, no 6mA incorporation into the MIC was detected, either during the old MAC degradation stage of late conjugation (with substantial endogenous 6mA supply) (*SI Appendix*, Fig. S2*L*), or upon feeding of adenine (N^6-methyladenine) to vegetatively growing cells (with substantial exogenous 6mA supply) (*SI Appendix*, Fig. S2*M*). Therefore, 6mA in *Tetrahymena* genomic DNA is exclusively dependent on the MTase activity.

We next examined 6mA distribution along Pol II-transcribed genes. In Δ*AMT6* and Δ*AMT7*, 6mA was still enriched toward the

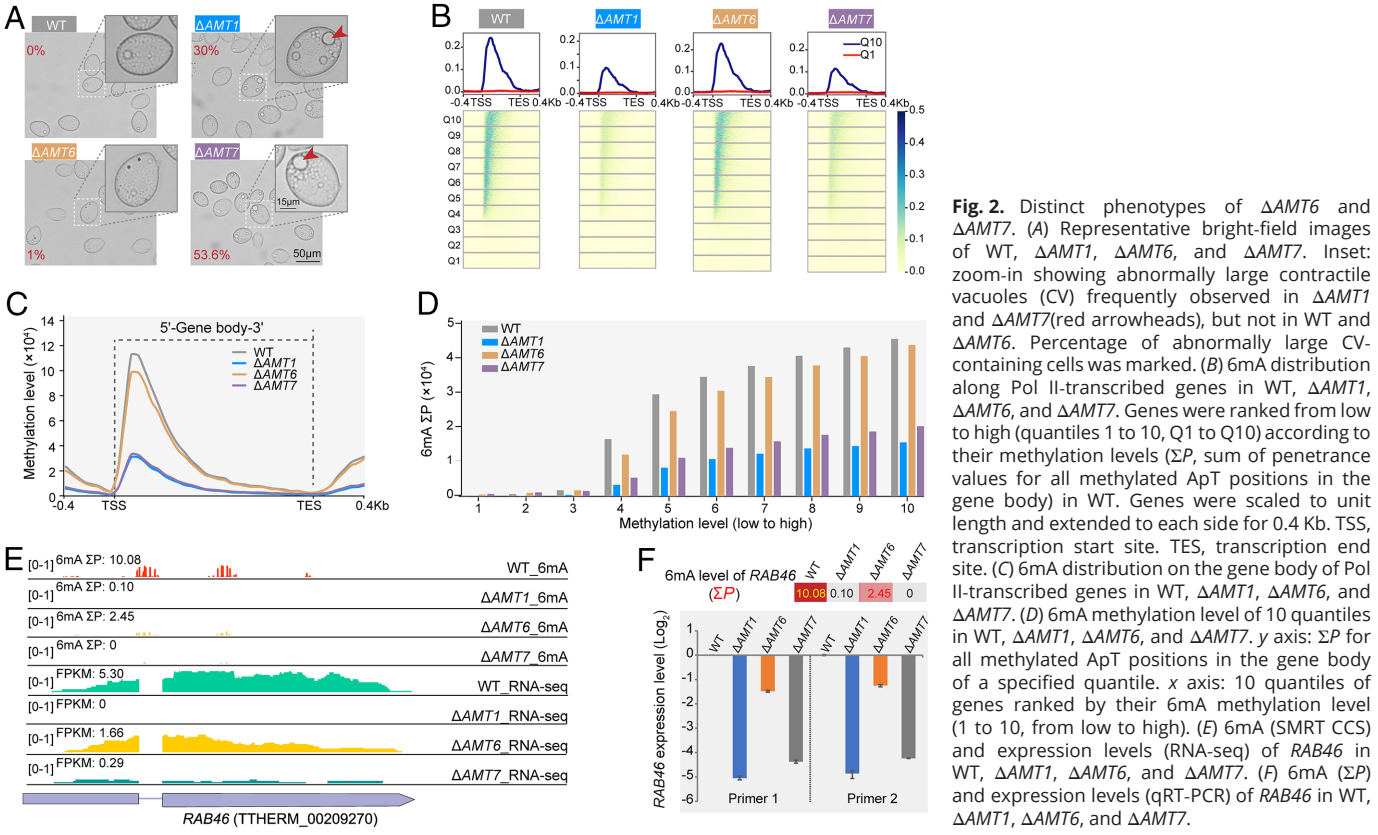

Fig. 2. Distinct phenotypes of Δ*AMT6* and Δ*AMT7*. (*A*) Representative bright-field images of WT, Δ*AMT1*, Δ*AMT6*, and Δ*AMT7*. Inset: zoom-in showing abnormally large contractile vacuoles (CV) frequently observed in Δ*AMT1* and Δ*AMT7*(red arrowheads), but not in WT and Δ*AMT6*. Percentage of abnormally large CV-containing cells was marked. (*B*) 6mA distribution along Pol II-transcribed genes in WT, Δ*AMT1*, Δ*AMT6*, and Δ*AMT7*. Genes were ranked from low to high (quantiles 1 to 10, Q1 to Q10) according to their methylation levels (Σ*P*, sum of penetrance values for all methylated ApT positions in the gene body) in WT. Genes were scaled to unit length and extended to each side for 0.4 Kb. TSS, transcription start site. TES, transcription end site. (*C*) 6mA distribution on the gene body of Pol II-transcribed genes in WT, Δ*AMT1*, Δ*AMT6*, and Δ*AMT7*. (*D*) 6mA methylation level of 10 quantiles in WT, Δ*AMT1*, Δ*AMT6*, and Δ*AMT7*. *y* axis: Σ*P* for all methylated ApT positions in the gene body of a specified quantile. *x* axis: 10 quantiles of genes ranked by their 6mA methylation level (1 to 10, from low to high). (*E*) 6mA (SMRT CCS) and expression levels (RNA-seq) of *RAB46* in WT, Δ*AMT1*, Δ*AMT6*, and Δ*AMT7*. (*F*) 6mA (Σ*P*) and expression levels (qRT-PCR) of *RAB46* in WT, Δ*AMT1*, Δ*AMT6*, and Δ*AMT7*.

5′ end of the gene body (Fig. 2 *B* and *C* and *SI Appendix*, Fig. S2*N*). 6mA levels across the gene body were slightly lower in Δ*AMT6* compared to WT; 6mA levels in Δ*AMT7* were much lower than WT, but slightly higher than Δ*AMT1* (Fig. 2 *B* and *C*). High-6mA genes in WT showed reduction in both Δ*AMT6* and Δ*AMT7*; the decrease was often much more severe in Δ*AMT7* than in Δ*AMT6* (Fig. 2 *B* and *D*). Notably, *RAB46*, encoding a Rab family GTPase regulating membrane fusion/fission (25, 26), contained substantial 6mA levels in WT and Δ*AMT6*, but lost almost all 6mA in Δ*AMT1* and Δ*AMT7* (Fig. 2 *E* and *F*). *RAB46* expression levels were also greatly diminished in Δ*AMT1* and Δ*AMT7*, relative to WT and Δ*AMT6* (Fig. 2 *E* and *F*). As RNAi knockdown of *RAB46* recapitulates the dysfunctional contractile vacuole phenotype of Δ*AMT1* (17), its disparate expression levels, attributable to its differential methylation, probably underpins the observed variations in the penetrance of the abnormal contractile vacuole phenotype (Fig. 2*A*).

Distinct 6mA Profiles in Δ*AMT6* and Δ*AMT7*. We further dissected contributions of AMT6 and AMT7 to maintenance methylation by comparing 6mA profiles in WT, Δ*AMT6*, and Δ*AMT7*. Importantly, we were able to distinguish between full-6mApT and hemi-6mApT by SMRT CCS (Fig. 3*A* and *SI Appendix*, Fig. S2*J* and Table S5). AMT1 is required for maintenance methylation that converts hemi-6mApT to full-6mApT (19). Upon *AMT1* deletion, almost all full-6mApT sites were lost (89.32% in WT vs. 3.03% in Δ*AMT1*) (Fig. 3*A* and *SI Appendix*, Table S5). The remaining 6mApT sites, almost all hemi-6mApT, are the product of AMT1-independent de novo methylation, catalyzed by AMT2 and AMT5 (27). In Δ*AMT7*, the total 6mApT level (full + hemi, relative to all ApTs) was reduced to that of Δ*AMT1* (1.89% in WT; 0.53% in Δ*AMT7*; 0.50% in Δ*AMT1*) (*SI Appendix*, Fig. S3*A* and Table S5). However, about half of its 6mApT sites were fully methylated (54.28% in Δ*AMT7* vs. 3.03% in Δ*AMT1*), apparently catalyzed by AMT6 complex. There was a strong overlap between genomic positions methylated in Δ*AMT7* and Δ*AMT1* (*SI Appendix*, Fig. S3*B*), indicating that the same set of ApT sites were targeted by AMT6 complex-dependent maintenance methylation (in Δ*AMT7*) and AMT1-independent de novo methylation (in Δ*AMT1*). These results support that in the absence of AMT7 complex, AMT6 complex is generally not sufficient to sustain full-6mApT levels across cell cycles (leading to eventual loss by passive dilution), except at sites that are also replenished by AMT1-independent de novo methylation. In contrast, when comparing Δ*AMT6* to Δ*AMT1*, we observed a much higher total 6mApT level (1.68% in Δ*AMT6*; 0.53% in Δ*AMT7*; 0.50% in Δ*AMT1*), a much lower hemi-6mApT level (16.72% in Δ*AMT6*; 45.72% in Δ*AMT7*; 96.97% in Δ*AMT1*), and much less overlap between methylated genomic positions (*SI Appendix*, Fig. S3 *A* and *B* and Table S5). These results support that in the absence of AMT6 complex, AMT7 complex is sufficient to sustain full-6mApT levels across cell cycles at most sites. Therefore, AMT7 complex plays a major role in maintenance methylation.

In WT, there were abundant DNA molecules containing many full-6mApT sites but few hemi-6mApT sites, while those of the opposite pattern were rare (Fig. 3 *B*, *Left*). By contrast, DNA molecules in Δ*AMT7* predominantly featured many hemi-6mApT but few full-6mApT; those of the opposite pattern were essentially absent (Fig. 3 *B*, *Right*). In Δ*AMT6*, both patterns were commonly found in DNA molecules (Fig. 3 *B*, *Middle*). These DNA molecules were from asynchronously growing cells, representing random sampling of cell cycle progression as well as MP. We characterized the MP profile by focusing on DNA molecules with multiple 6mApT sites (full and hemi). In WT, most DNA molecules were at or near complete hemi-to-full conversion and dominated by full-6mApT (late MP), while few were at initial conversion stages and dominated by hemi-6mApT (early MP) (Fig. 3*C*). This MP profile supports that maintenance methylation is initiated shortly after DNA replication and quickly cascades to completion in WT. By contrast, there were almost no DNA molecules at late MP in

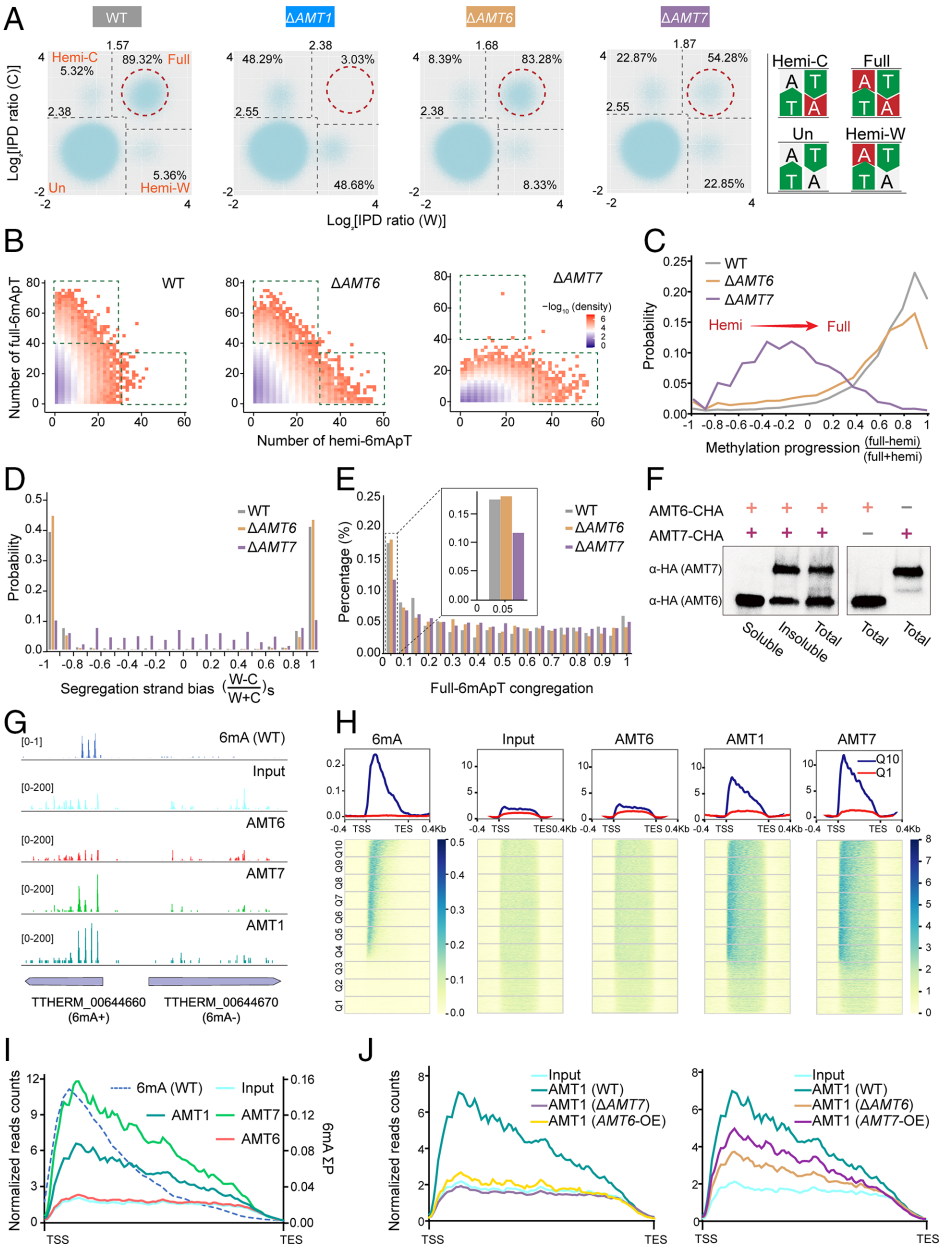

Fig. 3. Distinct methylation characteristics, chromatin affinity, and genomic distribution of AMT6 and AMT7. (*A*) Full-6mApT and hemi-6mApT levels in WT, Δ*AMT1*, Δ*AMT6*, and Δ*AMT7*. Note the abundance of full methylation in WT and Δ*AMT6*, but its absence in Δ*AMT1* and substantial reduction in Δ*AMT7*. (*B*) Two-dimensional (2D) distribution of all methylated DNA molecules in WT, Δ*AMT6*, and Δ*AMT7*, according to the number of hemi-6mApT (*x* axis) and full-6mApT sites (*y* axis) contained in each DNA molecule. (*C*) Methylation progression (MP) in WT, Δ*AMT6*, and Δ*AMT7*. MP was calculated as the difference-sum ratio between full-6mApT and hemi-6mApT on individual DNA molecules: $(\frac{\text{full}-\text{hemi}}{\text{full}+\text{hemi}})$. (*D*) Segregation strand bias in WT, Δ*AMT6*, and Δ*AMT7*, defined as the difference-sum ratio between hemi-6mApT sites on W and C: $(\frac{W-C}{W+C})_S$. (*E*) Full-6mApT congregation in DNA molecules undergoing hemi-to-full conversion in WT, Δ*AMT6*, and Δ*AMT7*. *x* axis: the probability for simulated max inter-full distances to be no greater than the observed value; *y* axis: the percentage of total DNA molecules with the corresponding probability. (*F*) Differential chromatin affinity of AMT6 and AMT7. AMT6 and AMT7 were fractionated by salt and detergent extraction (soluble and insoluble) and visualized by Immunoblot. (*G*) A representative genomic region showing distributions of AMT1, AMT6, and AMT7 along Pol II-transcribed genes in WT. Tracks (*Top* to *Bottom*): 6mA penetrance, ChIP input, AMT6, AMT7, and AMT1 ChIP, gene models: 6mA+ vs. 6mA− genes. (*H*) Distributions of 6mA, ChIP input, AMT1, AMT6, and AMT7 ChIP along the gene body in WT. The gene body, from TSS to TES, was normalized to unit length and extended in both directions by 0.4 kb. Pol II-transcribed genes (26,359 in total) were divided into 10 quantiles (Q1 to Q10: low-6mA level to high-6mA level) according to their mean methylation levels in WT. AMT1, AMT6, and AMT7 distributions were normalized by their read counts of Q1 in the gene body. Composite plot showed the distribution of Q1 and Q10. Heat map displayed all 10 quantiles. (*I*) 6mA, AMT1, AMT6, and AMT7 distributions from TSS and TES in Q10 (top quantile ranked by WT 6mA Σ*P*). Input was included as control for background. *y* axis: normalized read count (*Left* scale) and 6mA Σ*P* (*Right* scale). (*J*) AMT1 distribution along the gene body was affected by changing AMT6 or AMT7 levels, showcased for Q10. *Left*: AMT1 distribution in WT, *AMT6*-OE, and Δ*AMT7*. *Right*: AMT1 distribution in WT, *AMT7*-OE, and Δ*AMT6*.

Δ*AMT7* (Fig. 3*C*), which was not surprising given the abundance of hemi-6mApT sites and their random distribution (Fig. 2*D* and *SI Appendix*, Table S5). Instead, there were many DNA molecules at early MP (Fig. 3*C*), supporting slow methylation progression. MP distribution in Δ*AMT6* was more like WT, but less skewed toward completion (Fig. 3*C*). Meanwhile, there was accumulation at early MP in Δ*AMT6*, indicating a delay in initial methylation (Fig. 3*C* and *SI Appendix*, Fig. S3*C*). The altered 6mA profiles in Δ*AMT6* and Δ*AMT7* reveal distinct methylation characteristics of AMT6 and AMT7 complexes.

Semiconservative 6mA transmission entails that hemi-6mApT is only found on the parental strand immediately after replication, leading to strong segregation strand bias. Indeed, for DNA molecules at early MP, hemi-6mApT sites exhibited strong segregation strand bias in Δ*AMT6* as well as in WT (Fig. 3*D* and *SI Appendix*, Fig. S3*D*). However, their counterparts in Δ*AMT7* did not (Fig. 3*D*). This anomaly can be attributed to AMT1-independent de novo methylation (27, 28), a much slower reaction that is superseded by the fast maintenance methylation in WT, and only reveals itself when maintenance methylation is severely compromised in Δ*AMT7*.

Many maintenance MTases (e.g., *E. coli* Dam DNA MTase) are processive rather than distributive (29). We have previously shown that AMT1-dependent maintenance methylation is also processive (19). This was revealed by the congregation of full-6mApT sites in WT: For individual DNA molecules at early MP, the observed maximum distance between adjacent full-6mApT sites was often much smaller than expected (Fig. 3*E* and *SI Appendix*, Fig. S3*E*). Compared to WT, full-6mApT congregation was much reduced in Δ*AMT7*, but not in Δ*AMT6* (Fig. 3*E*). This supports that AMT7 complex contributes strongly to the processivity of maintenance methylation, while AMT6 complex is much less processive. This conclusion is consistent with the former's high affinity for DNA/chromatin and the latter's low affinity (see below).

Distinct Chromatin Affinity and Genomic Distribution of AMT6 and AMT7. We next characterized the chromatin association of AMT6 and AMT7. Under the same extraction condition, virtually all AMT7 remained chromatin-bound, while most AMT6 could be solubilized (Fig. 3*F*); AMT1 had a small soluble fraction and a large chromatin-bound fraction (*SI Appendix*, Fig. S3*F*). These

observations can be attributed to AMT7 complex's higher DNA binding affinity (*Differential Activities of Reconstituted AMT6 and AMT7 Complexes*) and its potentially higher affinities for other chromatin-associated proteins (*AMT7 Complex Is Recruited by Transcription-Associated Epigenetic Pathways*).

We performed chromatin immunoprecipitation (IP) followed by deep sequencing (ChIP-seq) to track genomic distribution of AMT1, AMT6, and AMT7 (Fig. 3 *G–I*). In WT, we found that reads recovered from AMT6 ChIP were rather evenly dispersed across the gene body and essentially the same as the input (Fig. 3 *G–I* and *SI Appendix*, Fig. S3 *G* and *H*), supporting that AMT6 binds chromatin with low affinity. In contrast, AMT7 ChIP reads were highly enriched toward the 5′ end of many Pol II-transcribed genes (Fig. 3 *G–I* and *SI Appendix*, Fig. S3*H*), a pattern reminiscent of 6mA distribution (Fig. 2 *B* and *C*). This supports that AMT7 binds chromatin selectively and with high affinity. AMT1 distribution was in an intermediate state (Fig. 3 *G* and *H*), closely fitted by linear combination of AMT6 and AMT7 distributions (Fig. 3*I* and *SI Appendix*, Fig. S3*H*).

We then examined AMT1, AMT6, and AMT7 distribution in 10 quantiles of Pol II-transcribed genes (Fig. 3*H* and *SI Appendix*, Fig. S3*G*), ranked lowest to highest by 6mA levels in WT (Fig. 2 *B* and *D*). AMT7 was enriched in high-6mA genes and almost completely depleted in low-6mA genes, while AMT6 was more evenly distributed across all genes (Fig. 3*H* and *SI Appendix*, Fig. S3*G*). Again, we found AMT1 distribution in an intermediate state, closely fitted by linear combination of AMT6 and AMT7 distributions (*SI Appendix*, Fig. S3 *H* and *I*). These results strongly suggest that AMT1 is partitioned between AMT6 complex with low chromatin affinity and AMT7 complex with high chromatin affinity.

We next examined how AMT1 distribution may be affected by changes in AMT6 or AMT7 levels (Fig. 3*J*). In addition to Δ*AMT6* and Δ*AMT7*, we also generated *Tetrahymena* strains overexpressing either AMT6 (*AMT6*-OE) or AMT7 (*AMT7*-OE) (*SI Appendix*, Fig. S3 *J* and *K*). In Δ*AMT7*, AMT1 was mostly found in the soluble fraction (*SI Appendix*, Fig. S3*F*). Moreover, AMT1 distribution along the gene body was no longer highly enriched at 5′ of the gene body, even for genes with the highest 6mA levels in WT (Fig. 3 *J*, *Left*); instead, AMT1 was distributed in a pattern very similar to AMT6 (Fig. 3*I*). As mentioned above, global 6mA level was greatly reduced in Δ*AMT7* (Fig. 2*D* and *SI Appendix*, Table S5), which may have been exacerbated by substantial reduction in both AMT1 and AMT6 levels (*SI Appendix*, Fig. S3*L*). Similar phenotypes were also observed upon overexpression of AMT6, including increased AMT1 solubility, fully dispersed genomic distribution, and reduced global 6mA level (Fig. 3 *J*, *Left* and *SI Appendix*, Fig. S3*K* and Table S6). Note that global AMT1 level was not substantially affected in *AMT6*-OE (*SI Appendix*, Fig. S3*L*), which may account for the less dramatic 6mA reduction than in Δ*AMT7*. These results support the repartition of AMT1 from AMT7 complex to AMT6 complex, which is driven by either lack of AMT7 or excess of AMT6, results in reduced chromatin affinity and specific binding of AMT1, as well as 6mA deposition.

The results were more complex when we tried to tilt the balance in the other direction. Global AMT1 level was not substantially affected upon overexpression of AMT7 (*SI Appendix*, Fig. S3*L*). However, a substantial portion of overexpressed AMT7 was soluble (*SI Appendix*, Fig. S3*M*) and AMT1 was also shifted from the chromatin-bound fraction to the soluble fraction (*SI Appendix*, Fig. S3*F*), suggesting that at least some AMT7 complex was no longer tightly chromatin-bound. Consistent with this interpretation, the ChIP result showed that AMT1 enrichment toward 5′ of the gene body was reduced (Fig. 3 *J*, *Right*). In Δ*AMT6*, AMT1 level remained stable, while AMT7 was substantially increased (possibly to compensate the loss of AMT6), incidentally achieving its overexpression (*SI Appendix*, Fig. S3*L*). There was also a surprisingly large pool of AMT7 (as well as AMT1) in the soluble fraction (*SI Appendix*, Fig. S3*M*), suggesting the presence of free AMT7 complex. Moreover, AMT1 distribution across the gene body was dispersed, but not to the extreme degree observed in Δ*AMT7* and *AMT6*-OE (Fig. 3*J*). Global 6mA level was not significantly affected in *AMT7*-OE and only slightly reduced in Δ*AMT6* (Fig. 2*D* and *SI Appendix*, Tables S5 and S6). We attribute these observations to (near) saturation of high-affinity binding sites by AMT7 complex in WT; excess AMT7 complex was driven into the soluble fraction. This may also explain their relatively minor effects on the global 6mA level.

AMT7 Complex Is Connected to Transcription-Associated Epigenetic Marks. Further analysis showed that AMT7 distribution was correlated with not only 6mA, but also other transcription-associated epigenetic marks, especially the histone posttranslational modification H3K4me3 and the histone variant H2A.Z (Fig. 4 *A–C*). Pairwise comparison showed that the levels of AMT7, as well as 6mA, H3K4me3, and H2A.Z, on Pol II-transcribed genes were strongly correlated with each other in vegetatively growing *Tetrahymena* cells (Fig. 4*C*). Indeed, most *Tetrahymena* genes were either enriched (triple+: 61.11%) or depleted for all three epigenetic marks (triple–: 26.97%) (*SI Appendix*, Fig. S4*A*). Moreover, all three marks showed strong correlations with gene expression levels (Fig. 4*C*). As conserved transcription-associated epigenetic marks, H3K4me3 and H2A.Z are known to play important roles in transcription regulation (30–33). The same designation and functional implication for 6mA are supported by the following results: 1) In WT cells, 6mA+ genes had significantly higher expression levels than 6mA– genes (*SI Appendix*, Fig. S4*B*). 2) In Δ*AMT1* cells, there was a substantial decrease in overall expression levels as well as 6mA levels (*SI Appendix*, Fig. S4 *C–E*). 3) Overexpression of AMT1 increases 6mA levels in AMT1 target genes and promotes their transcription (34). These results strongly support a positive role for 6mA in transcription regulation. However, as a stable epigenetic mark, 6mA may not change its levels in timely response to changes in gene expression. Indeed, despite the substantial decrease in overall gene expression during starvation, 6mA levels remained steady in *Tetrahymena* (*SI Appendix*, Fig. S4 *F–H*).

AMT7, 6mA, H3K4me3, and H2A.Z were all coenriched toward the 5′ end of Pol II-transcribed genes (Fig. 4 *A* and *B*), consistent with our previous reports (17). AMT7 was enriched on nucleosomes with high levels of H3K4me3 or H2A.Z (*SI Appendix*, Fig. S4*I*). 6mA levels were the highest for linker DNA flanked on both sides by such nucleosomes, much reduced if only flanked on one side, and minimal if not flanked at all (Fig. 4*D*). Among linker DNA flanked by two such nucleosomes, 6mA levels were high if both H3K4me3 and H2A.Z were enriched in both nucleosomes, but much reduced if either mark was depleted from either nucleosome (Fig. 4*E*). In addition, 6mA penetrance dropped precipitously in linker DNA significantly exceeding the regular length (*SI Appendix*, Fig. S4 *J* and *K*). All these observations suggest that 1) H3K4me3/H2A.Z-containing nucleosomes represent high-affinity sites for AMT7 complex; and 2) a pair of such nucleosomes, joined by 6mA-decorated linker DNA of proper length, is a basic unit for AMT7 complex-dependent 6mA transmission (Fig. 4*F*).

After establishing correlations between AMT7 and the triple marks in WT, we next investigated their response to perturbations. As H2A.Z is encoded by an essential gene in *Tetrahymena* (35), we focused on loss-of-function analyses of H3K4me3. In Δ*MLL1*, knocking out the only *Tetrahymena* homolog of mixed lineage leukemia (MLL/KMT2) family histone MTases (36), H3K4me3 global levels were greatly diminished (*SI Appendix*, Fig. S4 *L* and

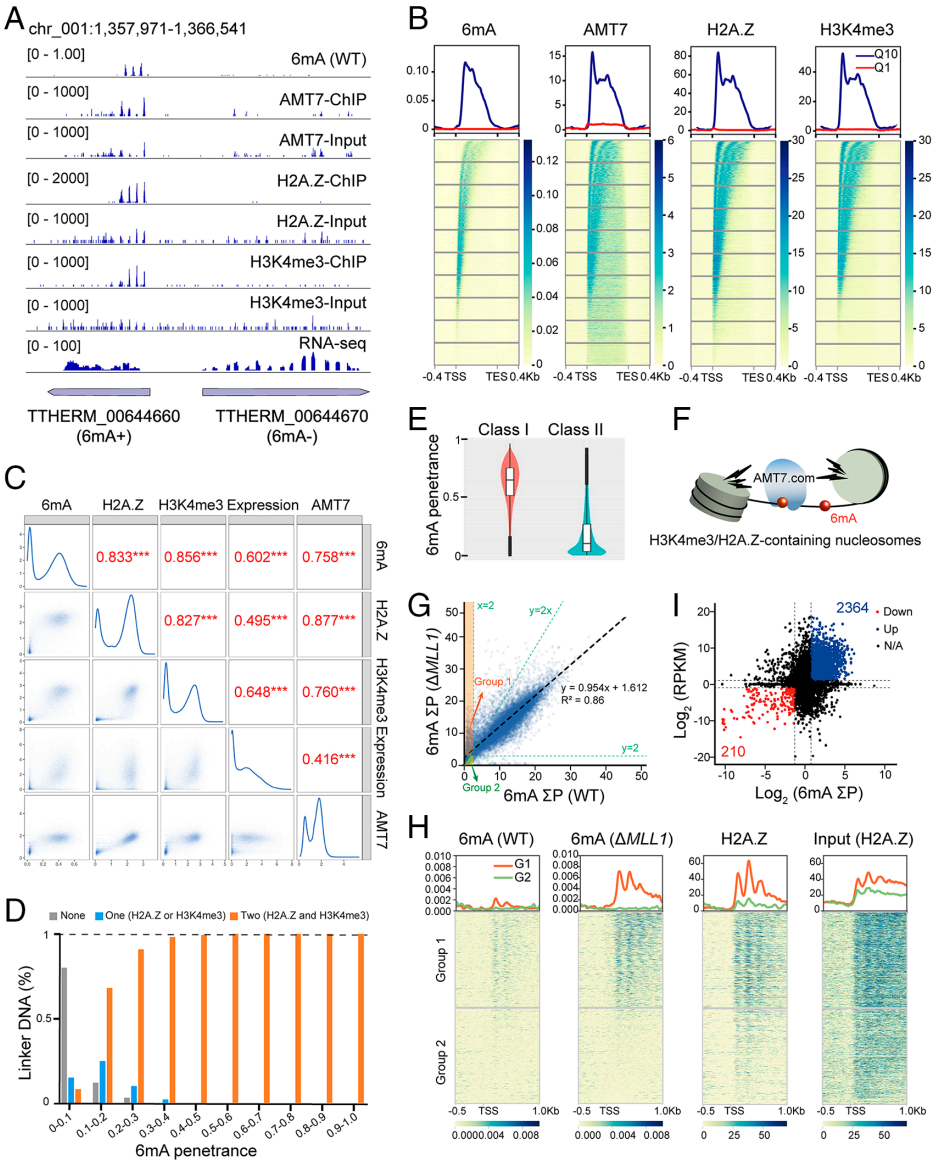

Fig. 4. The association of AMT7 and 6mA with transcription. (*A*) A representative genomic locus showing distributions of 6mA, AMT7, H2A.Z, and H3K4me3 as well as gene expression in WT. Note the difference in the abundance of epigenetic marks between two neighboring genes. 6mA+: high 6mA level; 6mA−: low 6mA level. (*B*) Distributions of 6mA, AMT7, H2A.Z, and H3K4me3 along the gene body in WT. Composite plot showed the distribution of Q1 and Q10. Heat map displayed all 10 quantiles. (*C*) Correlations between 6mA, H2A.Z, H3K4me3, AMT7, and gene expression levels. 6mA levels: 6mA Σ*P*. H2A.Z, H3K4me3, and AMT7 levels: ChIP reads normalized by input across the gene body. Gene expression levels: RPKM for RNA-seq of WT. (*D*) 6mA penetrance in linker DNA (LD) dependent on whether none, one, or two of the flanking nucleosomes were enriched for H2A.Z and/or H3K4me3. 6mA was divided into 10 groups according to their penetrance (*x* axis). The percentage of a specific type of LD in each 6mA group was calculated (*y* axis). (*E*) Higher 6mA penetrance in LD when each of the two flanking nucleosomes were enriched for both H2A.Z and H3K4me3 (Class I) than when one mark was missing from either nucleosome or both (Class II). (*F*) Model: AMT7 complex is targeted by the dinucleosome containing H2A.Z and H3K4me3 for efficient 6mA deposition on LD. (*G*) 6mA levels of individual genes in WT and Δ*MLL1*. In Δ*MLL1*, 6mA levels substantially increased in many WT low-6mA genes, while remained stable in most WT high-6mA genes (dotted diagonal line). Each gene was assigned a coordinate: 6mA Σ*P* for WT (*x* axis) and Δ*MLL1* (*y* axis). Group 1 were genes with low 6mA level in WT but elevated 6mA level in Δ*MLL1*: $\Sigma P(\Delta MLL1) \geq 2 \times \Sigma P(WT)$, $\Sigma P(\Delta MLL1) \geq 2$, $\Sigma P(WT) \leq 2$. Group 2 were genes with stably low 6mA level in both cells: $\Sigma P(\Delta MLL1) < 2 \times \Sigma P(WT)$, $\Sigma P(\Delta MLL1) < 2$, $\Sigma P(WT) \leq 2$. (*H*) 6mA in Δ*MLL1* spread to genomic regions moderately enriched for H2A.Z (G1, group 1 defined in *G*), but remained unaffected in regions devoid of H2A.Z (G2, group 2 defined in *G*). (*I*) Relationship between changes in 6mA and gene expression in WT and Δ*MLL1*. Δ*MLL1* vs. WT: Log_2(FoldChange) for individual genes in 6mA (*x* axis: Σ*P*) and expression (*y* axis: RPKM). Blue: genes with significantly increased 6mA and expression levels (>2×). Red: genes with significantly decreased 6mA and expression levels (<0.5×).

M). While 6mA global level and full-6mApT percentage in Δ*MLL1* were comparable to WT (*SI Appendix*, Fig. S4 *N* and *O* and Table S5), there were notable alterations to 6mA patterns (Fig. 4*G* and *SI Appendix*, Fig. S3 *C–E*). DNA molecules at early MP accumulated (*SI Appendix*, Fig. S3*C*), but the delay of initial methylation was not severe enough to affect the segregation strand bias of hemi-6mApT (*SI Appendix*, Fig. S3*D*).

6mA distribution across Pol II-transcribed genes was also altered in Δ*MLL1*. For high-6mA genes in WT, their 6mA levels were mostly unaffected; however, for low-6mA genes in WT, their 6mA levels were often substantially increased (Fig. 4 *G* and *H* and *SI Appendix*, Fig. S4 *P–R* and Table S7). Furthermore, while full-6mApT percentage was slightly reduced in Δ*MLL1* relative to WT for 6mA+ genes (78.01% and 80.74%, respectively), it was increased for 6mA– genes (58.55% and 41.38%, respectively) (*SI Appendix*, Table S7). This was not caused by random increases of methylation background in Δ*MLL1*: in Pol I-transcribed rDNA, 6mA remained at the minimum level (*SI Appendix*, Table S7); in genes with induced 6mA, 6mA distribution also oscillated with the 200-bp periodicity and exhibited a strong bias toward 5′ end of the gene body (Fig. 4*H* and *SI Appendix*, Fig. S4*S*). Therefore, while H3K4me3 is not required for 6mA (possibly due to redundancy in AMT7 complex recruitment mechanisms), it plays a crucial role in limiting off-target 6mA, likely via its contribution in recruiting and sequestering AMT7 complex. Intriguingly, genes with induced 6mA in Δ*MLL1* often had higher H2A.Z levels than those that remained 6mA-low (Fig. 4*H*), suggesting that even the off-target 6mA sites are not random, but rather biased toward genes decorated with H2A.Z.

We also examined gene expression changes in response to perturbations. Despite deficiency in the euchromatic mark H3K4me3, many genes were significantly up-regulated than down-regulated in Δ*MLL1* relative to WT (Fig. 4*I* and *SI Appendix*, Fig. S4*T*). This was especially prominent for 6mA– genes, many of which were expressed at the minimum level in WT but were induced in Δ*MLL1*, accompanied by significantly increased 6mA levels; their changes in gene expression levels showed positive correlations with changes in 6mA levels (Fig. 4*I*). In contrast, for many 6mA+ genes in WT, they showed minimum 6mA in Δ*AMT7*, while their expression was mostly reduced; genes with less extreme reduction in 6mA levels showed more divergent response in expression levels (*SI Appendix*, Fig. S4*U*). These results suggest that for many Pol II-transcribed genes, a threshold 6mA level may be required for their expression.

AMT7 Complex Is Recruited by Transcription-Associated Epigenetic Pathways. In addition to its core complex components, we also identified IBD2 as an AMT7-interacting protein (Fig. 5 *A* and *B*

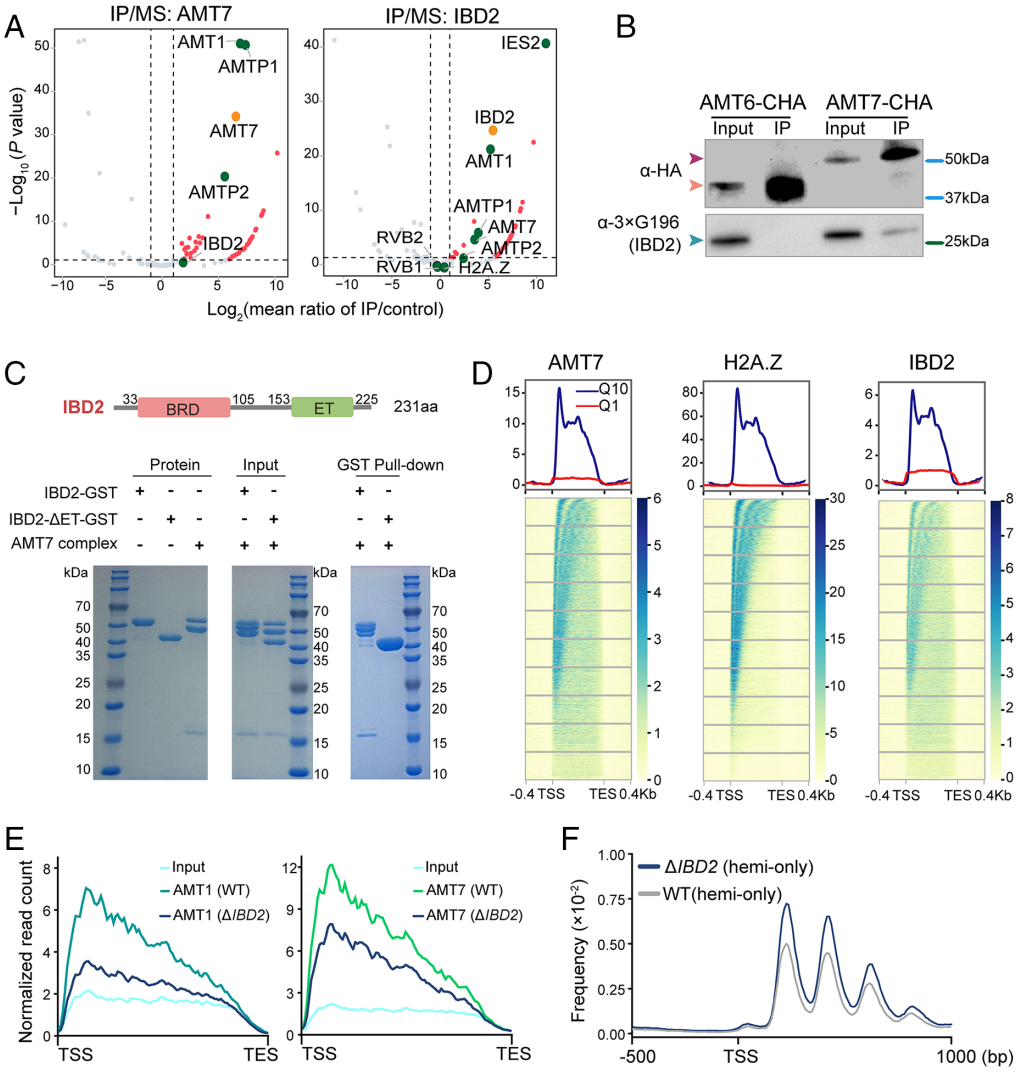

Fig. 5. AMT7 complex is recruited by transcription-associated epigenetic pathways. (*A*) Volcano plots of IP-MS results using AMT7 (*Left*) and IBD2 (*Right*) as bait, respectively. AMT7 specifically interacted with IBD2, INO80 complex, and H2A.Z. Bait: orange; high-confidence preys of interest: green; other high-confidence preys: red; low-confidence preys: gray. (*B*) IP-IB confirming the interaction of IBD2 with AMT7, but not AMT6. Bait proteins were tagged with a HA, while prey proteins were tagged with 3×G196. (*C*) Illustration of domain structures of IBD2 containing BRD (bromodomain) and ET (extra-terminal domain) and GST pull-down assay. The direct interaction between the IBD2-GST and AMT7 complex was disrupted by the deletion of the ET domain (IBD2-ΔET-GST). (*D*) Distributions of AMT7, H2A.Z, and IBD2 along the gene body in WT. AMT7, H2A.Z, and IBD2 distributions were normalized by input read counts of Q1 in the gene body. Composite plot showed the distribution of Q1 and Q10. Heat map displayed all 10 quantiles. (*E*) AMT1 (*Left*) and AMT7 (*Right*) distributions (Q10) along the gene body were affected by deleting *IBD2*, showcased for Q10 genes. (*F*) Accumulation of hemi-6mApT along the gene body in Δ*IBD2* relative to WT. *y* axis: 6mA frequency (6mA amount at a certain position/total 6mA amount).

and *SI Appendix*, Table S3). IBD2 contains a bromodomain near its N terminus and an ET (extraterminal) domain at its C-terminus, thus resembling BET family proteins in fungi and animals (Fig. 5*C* and *SI Appendix*, Fig. S5 *A* and *B*) (37, 38). Importantly, IBD2 was not pulled down with AMT6 (Fig. 5*B* and *SI Appendix*, Table S3). Reciprocally, IP with IBD2 as the bait pulled down AMT7 and its core complex components, but not AMT6 (Fig. 5*A* and *SI Appendix*, Table S8). The ET domain of IBD2 is known to function as a protein–protein interaction domain (39). To validate its role in AMT7 complex binding, we deleted the ET domain of IBD2 and assessed its interaction with AMT7 complex in vitro. IBD2 lacking the ET domain failed to pull down the AMT7 complex (Fig. 5*C*), confirming the essential role of the ET domain for this interaction. IBD2 also pulled down many other key players in transcription-associated epigenetic pathways, including RVB1, RVB2, IES2, and H2A.Z (Fig. 5*A* and *SI Appendix*, Table S8). RVB1 and RVB2, two highly conserved AAA+ ATPases, form a hetero-hexameric complex (40). Serving as a versatile protein–protein interaction platform, RVB1–RVB2 complex is shared by INO80, SWR1, and NuA4 complexes, which are respectively involved in incorporating H2A.Z into the nucleosome, evicting H2A.Z from the nucleosome, and acetylation of the H2A.Z-containing nucleosome (41, 42). IES2 is a conserved subunit specific for INO80 complex (43). Intriguingly, the repeat length of periodically distributed 6mA, reflecting the nucleosome repeat length, was slightly but consistently increased in Δ*AMT7* relative to WT, at both single molecule and ensemble levels (*SI Appendix*, Fig. S5 *C* and *D*). This change was also observed in Δ*AMT1* but not in Δ*AMT6* (*SI Appendix*, Fig. S5 *C* and *D*). We posit that the increase in nucleosome repeat length can be attributed to AMT7 complex' connection to INO80 complex, which plays a well-established role in regulating nucleosome positioning and linker DNA length (44, 45). Our results suggest that AMT7 complex may be recruited by these transcription-associated epigenetic pathways.

After establishing these connections in WT, we next investigated their response to perturbations. As RVB1–RVB2 complex and INO80 complex are essential in *Tetrahymena*, we focused our analysis on IBD2. Consistent with its potential role in regulating AMT7 complex-dependent 6mA deposition, IBD2 was also exclusively localized in the MAC (*SI Appendix*, Fig. S5*E*). Moreover, genomic distribution of IBD2 was strongly correlated with that of 6mA and AMT7, enriched at the 5′ end of the gene body (Fig. 5*D*). Indeed, 82.63% of genes enriched with IBD2 (15,999) were also enriched with both 6mA and AMT7 (*SI Appendix*, Fig. S5*F*). While the global level of AMT1 and AMT7 was not affected in Δ*IBD2* (*SI Appendix*, Fig. S5*G*), their enrichment at the 5′ end of the gene body was decreased (Fig. 5*E*). Moreover, IBD2 enrichment at the 5′ end was also decreased in Δ*AMT1* and Δ*AMT7* (*SI Appendix*, Fig. S5*H*), with the global level of IBD2 remaining unaffected (*SI Appendix*, Fig. S5*G*), suggesting the recruitment of IBD2 and AMT7-complex are mutually dependent.

Total 6mApT levels were essentially identical in WT and Δ*IBD2* (1.9%) (*SI Appendix*, Fig. S5 *I* and *J* and Table S5). They also shared very similar 6mA distribution profiles (*SI Appendix*, Fig. S5 *K* and *L*). However, hemi-6mApT percentage was substantially increased in Δ*IBD2* (Δ*IBD2*: 14.4%; WT: 10.7%) (*SI Appendix*, Table S5). The increased hemi-6mApT was evenly distributed along the gene body and among individual Pol II-transcribed genes (Fig. 5*F*). We also observed a substantial delay in early MP in Δ*IBD2* (*SI Appendix*, Fig. S3*C*). In other words, DNA molecules with many hemi-6mApT and few full-6mApT accumulated in Δ*IBD2* (*SI Appendix*, Fig. S3*C*). We found similar hemi-6mApT accumulation and MP delay in Δ*MLL1* (*SI Appendix*, Figs. S3*C* and S5*M*), suggesting that both IBD2 and MLL1 may promote AMT7 complex recruitment and its subsequent engagement with the DNA substrate. Additionally, full-methylation congregation was increased in both Δ*IBD2* and Δ*MLL1* (*SI Appendix*, Fig. S3*E* and S5*N*). This is attributable to reduced recruitment of AMT7 complex, which in turn reduces the probability for multiple copies of AMT7 complex to simultaneously and dispersively deposit 6mA on a single DNA molecule.

AMT6 Complex Is Recruited by PCNA and Important for Initiation of Maintenance Methylation after DNA Replication. In addition to its core complex components, we also identified PCNA, the key loading platform in DNA replication (46, 47), as an AMT6-interacting protein (Fig. 6 *A*, *Left* and *SI Appendix*, Table S3). PCNA was not pulled down with AMT7 (*SI Appendix*, Table S3). Reciprocal IP with PCNA as the bait pulled down AMT6 and its core complex components, but not AMT7 (Fig. 6 *A*, *Right* and *SI Appendix*, Table S9). These results demonstrate that PCNA specifically recruits AMT6 complex.

The interaction between AMT6 and PCNA was disrupted by mutating the PCNA-interacting protein (PIP)-box in AMT6 (*AMT6*-PIP: F176A, F187A) (Fig. 6 *B–D* and *SI Appendix*, Table S10). We also found that PIP-box was highly conserved in AMT6 homologs, but not in AMT7 (Fig. 6*E*). AF3 modeling predicted with high confidence that the PIP-containing loop of AMT6 (EKKITDFFKR) fit tightly into the hydrophobic cavity created by interdomain connecting loop of PCNA (Fig. 6*F*). Moreover, PCNA was also evenly distributed along the gene body, in a pattern like AMT6 (*SI Appendix*, Fig. S6*A*). All this prompted us to examine whether the AMT6–PCNA interaction was required for its 6mA deposition activity. Indeed, we found that *AMT6*-PIP largely phenocopied Δ*AMT6*. 6mA global level was moderately reduced, as quantified by MS and SMRT CCS (6mApT/all ApT; WT: 1.9%; Δ*AMT6*: 1.7%; *AMT6*-PIP: 1.6%) (*SI Appendix*, Fig. S6 *B–E* and Table S5). Moreover, there was a substantial increase in hemi-6mApT (hemi-6mApT/all 6mApT; WT: 10.7%; Δ*AMT6*: 16.7%; *AMT6*-PIP: 20.2%) (*SI Appendix*, Table S5), which was evenly distributed along the gene body (Fig. 6*G*) and among Pol II-transcribed genes (*SI Appendix*, Fig. S6*F*). Importantly, the PIP mutation did not affect AMT6 protein level or its MAC localization (*SI Appendix*, Fig. S6 *G* and *H*). Moreover, *AMT6*-PIP retained its ability to interact with AMT1, AMTP1, and AMTP2 (Fig. 6*B* and *SI Appendix*, Table S10), and *AMT6*–PIP complex could still methylate DNA in vitro (*SI Appendix*, Fig. S6*I*). Interestingly, AMT7 protein level increased substantially in Δ*AMT6* (*SI Appendix*, Fig. S3*L*)—probably as a compensatory response to shift from AMT6 complex to AMT7 complex—but not in *AMT6*-PIP (*SI Appendix*, Fig. S6*G*). This may explain the more severe effect on hemi-6mApT observed in *AMT6*-PIP than Δ*AMT6* (Fig. 6*G* and *SI Appendix*, Table S5). Taken together, these findings indicate that the interaction between AMT6 and PCNA is required for AMT6 complex to play a role in maintenance methylation.

DNA molecules with many hemi-6mApT and few full-6mApT were rare in WT but accumulated in Δ*AMT6* and *AMT6*-PIP (Fig. 6*H*). Correspondingly, we observed a substantial delay at the early stages of MP (Fig. 6*I* and *SI Appendix*, Fig. S3*C*). Importantly, DNA molecules with all hemi-6mApT sites showed strong segregation strand bias in these two AMT6 loss-of-function mutants as well as WT (*SI Appendix*, Fig. S3*D*). These DNA molecules are therefore generated by DNA replication splitting full-6mApT into hemi-6mApT. Delay in their processing strongly suggests that methylation by AMT6 complex, dependent on its interaction with PCNA, is important for initiation of maintenance methylation after DNA replication. As PCNA is loaded onto DNA during replication (48), its transient presence thereafter may mark the newly replicated DNA and provide a critical window for maintenance methylation.

Discussion

AMT6 and AMT7 Complexes Achieve Specific Methylation via Multiple Recognitions. In *Tetrahymena*, 6mA is transmitted in an AMT1-dependent semiconservative manner (19). Here, we characterize two AMT1 complexes, with AMT6 and AMT7 as their mutually exclusive components. Both AMT6 and AMT7 complexes prefer hemimethylated over unmethylated ApT sites as the substrate, consistent with their roles in maintenance methylation. However, they are recruited by different protein–protein interactions (PPI) and feature distinct MTase activities.

AMT7 complex targeting is mediated by transcription-associated epigenetic pathways. Here, we highlight H2A.Z as a nexus of these interactions. H2A.Z is enriched downstream of transcription start sites (TSS), where it is associated with active epigenetic marks like H3K4me3 and histone acetylation (3, 49–54). In *Tetrahymena*, most genes are either simultaneously marked by 6mA, H2A.Z, and H3K4me3 (triple+: 61.11%), or do not have any (triple–: 26.97%). Therefore, the triple marks may underpin the transcription-associated epigenetic landscape. We propose that a pair of H3K4me3/H2A.Z-containing nucleosomes, joined by 6mA-decorated linker DNA of proper length, represent a high-affinity site for AMT7 complex and a basic unit for AMT7 complex-dependent 6mA transmission. It is worth noting that AMT7 complex remains sequestered at these high-affinity sites even after completion of maintenance methylation. This may help to prevent nonspecific methylation across the rest of the genome.

AMT6 complex targeting is mediated by PCNA. PIP-box, mediating protein interactions with PCNA (55), is highly conserved in AMT6 homologs, but not AMT7. While the total 6mA level and the final methylation state of individual DNA molecules are little affected in Δ*AMT6* and *AMT6*-PIP, there is substantial delay in methylation progression, especially at the early stage, leading to accumulation of DNA molecules with many hemi-6mApT but few full-6mApT. AMT6 complex therefore plays a role in timely restoration of the 6mA pattern after DNA replication. Restoring the epigenetic landscape after DNA replication is a central problem in epigenetics and extensively studied (56–58). Intriguingly, for both 6mA and 5mC, restoration is expedited by PCNA (55), which stays transiently on newly replicated DNA and provides a critical window for maintenance methylation.

AMT6 complex mainly functions at the initiation of maintenance methylation, with minimal effect during late methylation progression due to the stronger MTase activity of AMT7 complex. In contrast, AMT7 complex impacts both the early and late methylation stages. IBD2, an AMT7 complex-interacting protein,

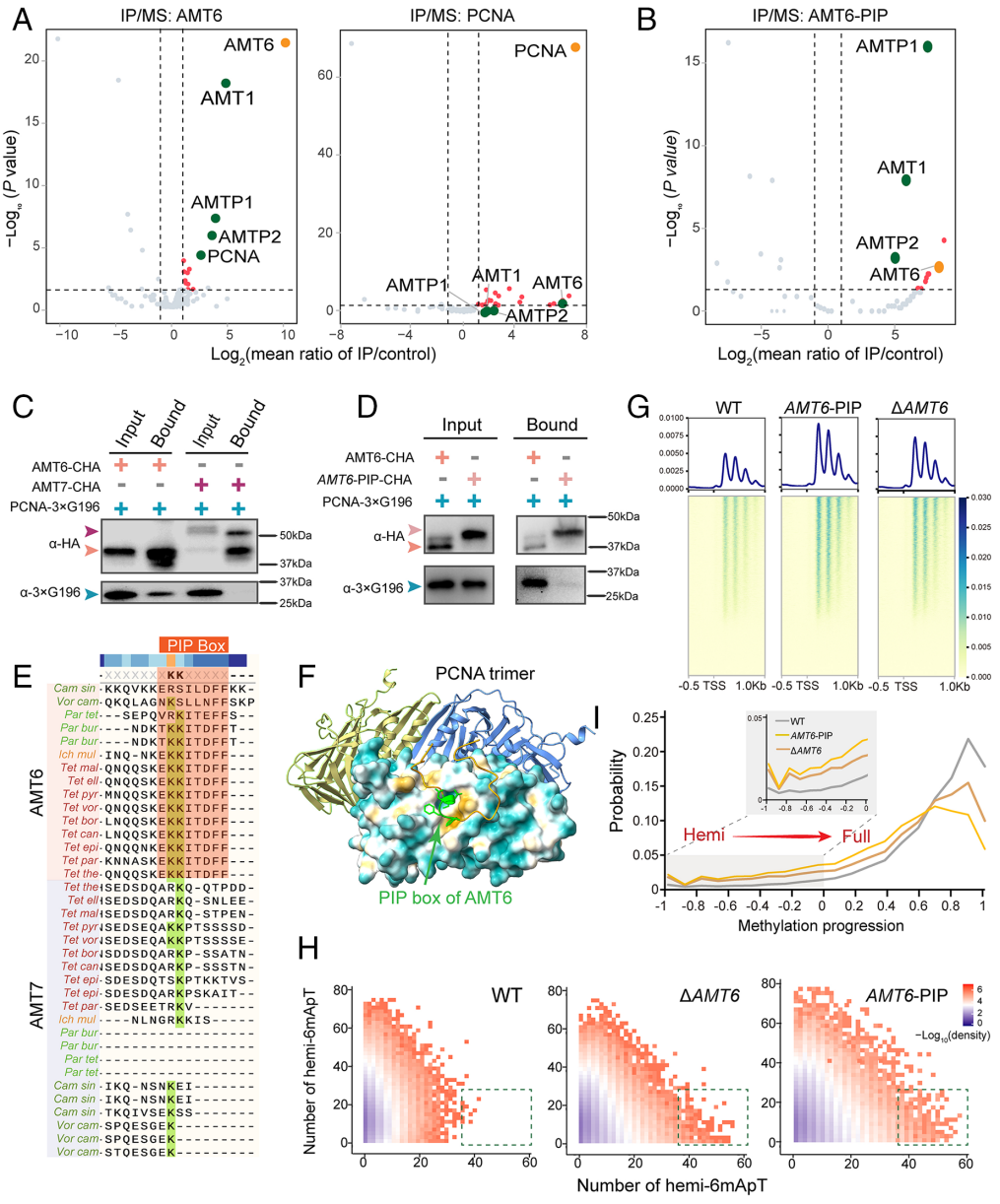

Fig. 6. AMT6 complex is recruited by PCNA and important for initiation of maintenance methylation after DNA replication. (*A*) Volcano plots of IP-MS results using AMT6 and PCNA as bait. AMT6 specifically interacted with PCNA. Bait: orange; high-confidence preys of interest: green; other high-confidence preys: red; low-confidence preys: gray. (*B*) Volcano plots of IP-MS results using *AMT6*-PIP as the bait. PIP mutation disrupted the interaction between AMT6 and PCNA interaction, but did not affect the integrity of AMT6 complex. (*C*) IP-IB confirming the interaction of PCNA with AMT6, but not AMT7. Bait proteins were tagged with a HA, while prey proteins were tagged with 3×G196. (*D*) IP-IB confirming that PIP mutation of AMT6 disrupted the interaction of PCNA with AMT6. Bait proteins were tagged with a HA, while prey proteins were tagged with 3×G196. (*E*) Sequence alignment of AMT6 and AMT7 homologs in ciliates. PIP was only conserved in AMT6 homologs but not AMT7 homologs. (*F*) AF3 prediction of the interaction between PCNA trimer and the PIP box of AMT6. The PIP-containing loop of AMT6 (EKKITDFFKR, shown in Lime stick) fit tightly into the hydrophobic cavity created by interdomain connecting loop of PCNA, with its surface colored by hydrophobicity. The molecular surface of PCNA are shown with coloring ranging from dark cyan (most hydrophilic) to white to dark goldenrod (most lipophilic). (*G*) Heat maps (*Bottom*) and composite plot (*Top*) showing increased hemi-6mApT downstream of TSS in *AMT6*-PIP. Composite plot showed the hemi-6mApT frequency. Heat map displayed all the well-annotated genes ranked by hemi-6mApT frequency (high to low). (*H*) 2D distribution of all methylated DNA molecules in WT, Δ*AMT6*, and *AMT6*-PIP. In Δ*AMT6* and *AMT6*-PIP, accumulation of DNA molecules at the bottom right corner (relative to WT), corresponding to early methylation progress. (*I*) MP in WT, Δ*AMT6*, and *AMT6*-PIP. DNA molecules at early MP accumulated in Δ*AMT6* and *AMT6*-PIP. *Left*: full plot. *Right*: zoom-in.

influences the enrichment of the AMT7 complex toward the 5′ end of the gene body. The weak phenotype of Δ*IBD2*, primarily defective mostly in methylation initiation, may be due to compensation by IBD1, a closely related BET protein involved in epigenetic regulation of transcription by interacting with chromatin remodeling complexes SWI/SNF and SWR, H3K4 methyltransferase TXR3, and histone acetyltransferase SAGA complexes in *Tetrahymena* (37). Future research will dissect distinct and overlapping roles of IBD1 and IBD2 in regulating transcription-associated 6mA deposition.

In summary, maintenance methylation in *Tetrahymena* can integrate signals from both replication and transcription, and achieve highly specific targeting of linker DNA marked by hemi-6mApT clusters, loaded with PCNA, and flanked by nucleosomes with transcription-associated epigenetic marks including H2A.Z and H3K4me3 (Fig. 7, *Top*).

AMT6 and AMT7 Complexes Coordinate in Maintenance Methylation. In *Tetrahymena*, 6mA, predominantly in the form of full-6mApT, is found at specific genomic regions, as a result of AMT1-dependent maintenance methylation (19). Here, we delineate several key steps for targeting two AMT1 complexes, with AMT6 and AMT7 as their unique components, respectively. AMT6 and AMT7 are recruited by separate PPI. For AMT6, the PIP box, required for its interaction with PCNA, resides in a flexible internal loop. The specific region of AMT7 required for its interaction with the ET domain of IBD2 has not yet been defined, but it is likely in the flexible N-terminal tail or internal loop, where AMT6 and AMT7 sequences diverge (*SI Appendix*, Fig. S1*F*). Their recruitment is followed by the assembly of AMT6 and AMT7 complexes on target sites. AMT6 and AMT7 compete for the same pool of AMT1 (most likely in the form of AMT1 subcomplex). AMT6 and AMT7 may even co-occupy target sites, actively exchange AMT1 subcomplex, and directly coordinate their methylation reactions. Our perturbation analyses support that AMT6 and AMT7 levels in WT *Tetrahymena* are (near) optimal for 6mA maintenance methylation. AMT7 is expressed at a level to (nearly) saturate high-affinity sites, but not in excess to drive AMT7 complex into the soluble fraction. AMT6 is expressed at a level to expedite maintenance methylation, but not in excess to compete away AMT7 complex binding at high-affinity sites. Indeed, maintenance methylation is negatively affected by deletion or overexpression of both AMT6 and AMT7. This finetuning

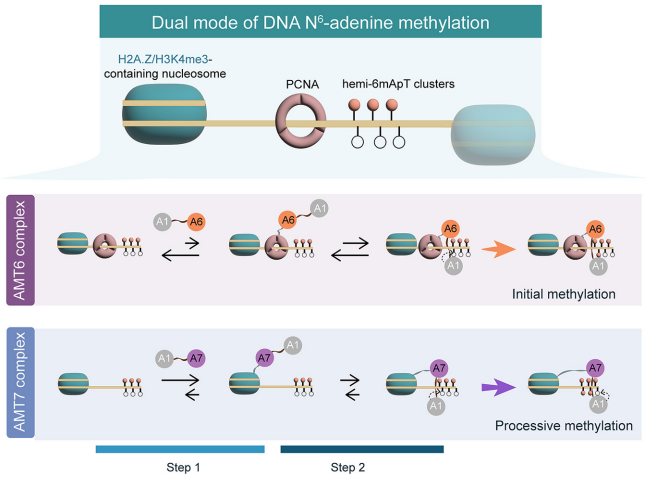

Fig. 7. AMT6 and AMT7 complexes coordinate in 6mA transmission. *Top*: Multiple recognition that integrates signals from both replication and transcription to achieve specific methylation, including hemi-6mApT, PCNA, H2A.Z, H3K4me3, and possibly other transcription-associated epigenetic marks. *Bottom*: AMT6 and AMT7 are both required for efficient initiation of methylation after DNA replication, while AMT7 is required throughout methylation progression. AMT6 MTase activity is required for dissociative priming and AMT7 MTase activity is required for processive expansion.

suggests that the balance between the two MTase complexes is tightly regulated and functionally relevant. We conclude that mediated by multiple recognitions, AMT6 and AMT7 complexes coordinate in maintenance methylation, to achieve specific, efficient, and robust transmission of 6mA as a eukaryotic epigenetic mark.

The AMT1-AMT7 heterodimeric core and its extension, comprising the N-terminal helix of AMT1, AMTP2, and the helix–turn–helix-like domain of AMTP1, are resolved in recent structural studies (20, 23). However, the DBD of AMTP1 remains elusive. Based on structure modeling by Alphafold3 (AF3), we posit that AMTP1 DBD has a specific local structure, but is connected to the rigid core/extension by a flexible linker sequence. In this way, the AMT7 apo-complex can sample a wide range of conformational states, most of them representing various open forms with AMTP1 DBD far away from AMT7. Intriguingly, upon binding the dsDNA substrate, AMTP1 DBD assumes a well-defined global relationship in the AMT7 holo-complex: It is placed in proximity to AMT7, while its recognition helix is aligned in the major groove opposite the target adenine site. In this conformation, AMT7, AMT1, and AMTP1 wrap around dsDNA and form a fully closed clamp, likely representing the active state for maintenance methylation. Ultimately, the closed form of the AMT7 holo-complex is established on linker DNA flanked by nucleosomes with a proper combination of epigenetic marks (Fig. 7, *Bottom*). Flexible tethering, combined with the presence of multiple binding sites (e.g., multiple acetyl-lysine sites for IBD2 binding and AMT7 tethering), may promote processive methylation by AMT7 complex. Similar transitions between the open and closed forms, driven by dsDNA binding, are also observed in the AMT6 apo/holo-complexes. The much higher DNA/chromatin affinity as well as MTase activity observed for AMT7 complex over AMT6 complex are probably underpinned by the structural and dynamic details that distinguish the two complexes, which will be explored in future studies.

Materials and Methods

Cell Culture. *T. thermophila* WT strains (SB210 and CU428) were obtained from the *Tetrahymena* Stock Center (http://tetrahymena.vet.cornell.edu). Homozygous homokaryon strain Δ*AMT1* and somatic HA tagged strains (AMT1-NHA and AMT7-CHA) were generated in our previous studies (17, 19, 59). Strains generated in this study are listed in *SI Appendix*, Table S11. Methods for strain generation in this study were described in *SI Appendix, Materials and Methods*. All primers used in this study are listed in *SI Appendix*, Table S12.

IP, In Vitro Cross-Linking, and Mass Spectrometry Analysis. Approximately 5×10^7 purified MACs were solubilized with 500 U Benzonase (Millipore, 712053N) and incubated with prewashed HA beads (Sigma, E6779). Targeted proteins were detected by mass spectrometry in Analysis Center of Agrobiology and Environmental Sciences, Zhejiang University.

The detailed methods are described in *SI Appendix, Materials and Methods*.

Methyltransferase Assay. For nonradioactive MTase assay, 2 μM protein was mixed with 1 μg pUC19 plasmid purified from *dam*$^-$/*dcm*$^-$ *E. coli*, 10 μM SAM in 40 μL reaction buffer. Samples were incubated at 30 °C for 30 min and inactivated at 65 °C for 20 min. Methylated DNA samples were treated with *Dpn*I at 37 °C for 30 min. For radioactive MTase assay, 0.05 μM protein was mixed with 0.5 μM [^{3}H]SAM and dsDNA at various concentrations. Samples were incubated at 30 °C for 30 min and subsequently spotted onto Hybond-XL membrane (GE Healthcare). Each membrane was immersed in Ultima Gold (PerkinElmer) and used for scintillation counting on a PerkinElmer MicroBeta2 (PerkinElmer). The DNA substrate for EMSA and SPR are listed in *SI Appendix*, Table S13.

Structure Prediction by AF3. All structural predictions, including AMT6 apo-complex, AMT6-holo complex with a dsDNA substrate, AMT7 apo-complex, AMT7-holo complex with a dsDNA substrate, and PCNA trimer with the PIP box of AMT6 were performed using the AF3 web server (https://alphafoldserver.com/), generating 50 predicted structures (10 samples with different seeds, five predicted structures per seed). The top five ranked structures for each complex were selected for further analysis. Input sequences for AF3 modeling are listed in *SI Appendix*, Table S14.

All the AF models included in the manuscript, as well as the validation results, can be retrieved from https://github.com/yefei521/AMT67/releases.

RNA-seq and ChIP-seq Data Analysis. RNA samples and ChIP samples were sequenced by Illumina HiSeq platform with 150 bp dual end sequencing. For RNA-seq, differentially expressed genes were identified by DESeq2 [$\mathrm{Log_2}$(FoldChange) > 1 or < −1, $P < 0.05$]. For ChIP-seq, the MACs of HA-tagged strains were purified and digested according to established protocols (60). Well-annotated Pol II-transcribed genes (26,359 in total) were scaled to unit length and divided into 10 quantiles (Q1 to Q10: low-6mA level to high-6mA level) according to their methylation levels per unit length. Each group from Q1 to Q10 was normalized using the area under the curve from TSS to TES of the Q1 group. Enriched genes were defined as ChIP/input ratio higher than 1 (normalized by total counts respectively). The detailed parameters are described in *SI Appendix, Materials and Methods*.

SMRT Sequencing and Data Analysis. SMRT sequencing data were analyzed following previously described procedures, including gene methylation level analysis, methylation progress, segregation strand bias, full-6mApT congregation, autocorrelation, and cross-correlation analysis (19). The detailed parameters are described in *SI Appendix, Materials and Methods*.

Data, Materials, and Software Availability. The latest SB210 MAC genome can be found at the *Tetrahymena* genome database (TGD) (http://ciliate.org) (61, 62). Accession number for publicly available *Tetrahymena* datasets: BioProject PRJNA1048849. AF3 predicted models and cross-linking mass spectrometry data: https://github.com/yefei521/AMT67/releases.

ACKNOWLEDGMENTS. This work was supported by the National Natural Science Foundation of China (32125006 to S.G., 32200399 to Y.W.), Natural Science Foundation of Shandong Province of China (ZR2024ZD40 to S.G., ZR2024MC112 to Y.W.), Young Talent of Lifting engineering for Science and Technology in Shandong, China (SDAST2024QTA008 to Y.W.), the Fundamental Research Funds for the Central Universities (202441014 to Y.W.), and National Science Foundation (MCB-2435178 to Yifan Liu). We would like to thank the following people and labs for assistance with this study: Prof. Zihe Rao, Prof. Zhiyong Lou, and Dr. Yunxiang Yang (Tsinghua University) for support with protein purification and methyltransferase assay; Dr. Kensuke Kataoka (National Institute for Basic Biology, Japan) for sharing the 3×G196 construct; Mr. Zhaorui Zhou (Ocean

University of China, OUC) for sharing the methods of phylogenetic tree construction; Prof. Haiteng Deng and Dr. Xianbin Meng (Proteomics Facility at Technology Center for Protein Sciences, Tsinghua University) for cross-linking mass spectrometry. Our special thanks are given to Dr. Weibo Song (OUC) for his helpful suggestions during drafting the manuscript. High-performance computing resources for data processing were provided by the High-Performance Biological Supercomputing Center, Marine Big Data Center of Institute for Advanced Ocean Study, and the Institute of Evolution and Marine Biodiversity at OUC, and the Center for Advanced Research Computing (CARC) at the University of Southern California.

1. M. A. Sanchez-Romero, I. Cota, J. Casadesus, DNA methylation in bacteria: From the methyl group to the methylome. *Curr. Opin. Microbiol.* **25**, 9–16 (2015).
2. M. Bochtler, H. Fernandes, DNA adenine methylation in eukaryotes: Enzymatic mark or a form of DNA damage? *Bioessays* **43**, e2000243 (2021).
3. Y. Wang, X. Chen, Y. Sheng, Y. Liu, S. Gao, N^6-adenine DNA methylation is associated with the linker DNA of H2A.Z-containing well-positioned nucleosomes in Pol II-transcribed genes in *Tetrahymena*. *Nucleic Acids Res.* **45**, 11594–11606 (2017).
4. Y. Fu *et al.*, N^6-methyldeoxyadenosine marks active transcription start sites in Chlamydomonas. *Cell* **161**, 879–892 (2015).
5. S. J. Mondo *et al.*, Widespread adenine N^6-methylation of active genes in fungi. *Nat. Genet.* **49**, 964–968 (2017).
6. E. L. Greer *et al.*, DNA methylation on N^6-adenine in *C. elegans*. *Cell* **161**, 868–878 (2015).
7. M. J. Koziol *et al.*, Identification of methylated deoxyadenosines in vertebrates reveals diversity in DNA modifications. *Nat. Struct. Mol. Biol.* **23**, 24–30 (2016).
8. Z. Liang *et al.*, DNA N(6)-adenine methylation in *Arabidopsis thaliana*. *Dev. Cell* **45**, 406–416 (2018).
9. J. Liu *et al.*, Abundant DNA 6mA methylation during early embryogenesis of zebrafish and pig. *Nat. Commun.* **7**, 13052 (2016).
10. X. Wang *et al.*, DNA methylation on N^6-adenine in lepidopteran *Bombyx mori*. *Biochim. Biophys. Acta Gene Regul. Mech.* **1861**, 815–825 (2018).
11. T. P. Wu *et al.*, DNA methylation on N(6)-adenine in mammalian embryonic stem cells. *Nature* **532**, 329–333 (2016).
12. C. L. Xiao *et al.*, N(6)-methyladenine DNA modification in the human genome. *Mol. Cell* **71**, 306–318 (2018).
13. G. Zhang *et al.*, N^6-methyladenine DNA modification in *Drosophila*. *Cell* **161**, 893–906 (2015).
14. C. Zhou *et al.*, Identification and analysis of adenine N(6)-methylation sites in the rice genome. *Nat. Plants* **4**, 554–563 (2018).
15. C. Lyu *et al.*, Rare and misincorporated DNA N(6)-methyladenine is a hallmark of cytotoxic stresses for selectively stimulating the stemness and proliferation of glioblastoma cells. *Cell Discov.* **8**, 39 (2022).
16. L. Y. Beh *et al.*, Identification of a DNA N^6-adenine methyltransferase complex and its impact on chromatin organization. *Cell* **177**, 1781–1796 (2019).
17. Y. Wang *et al.*, A distinct class of eukaryotic MT-A70 methyltransferases maintain symmetric DNA N^6-adenine methylation at the ApT dinucleotides as an epigenetic mark associated with transcription. *Nucleic Acids Res.* **47**, 11771–11789 (2019).
18. G. Z. Luo *et al.*, N(6)-methyldeoxyadenosine directs nucleosome positioning in *Tetrahymena* DNA. *Genome Biol.* **19**, 200 (2018).
19. Y. Sheng *et al.*, Semi-conservative transmission of DNA N^6-adenine methylation in a unicellular eukaryote. *Genome Res.* **34**, 740–756 (2024).
20. J. Yan *et al.*, Structural insights into DNA N^6-adenine methylation by the MTA1 complex. *Cell Discov.* **9**, 8 (2023).
21. Y. Wang *et al.*, N^6-methyladenine DNA modification in the unicellular eukaryotic organism *Tetrahymena thermophila*. *Eur. J. Protistol.* **58**, 94–102 (2017).
22. L. M. Iyer, D. Zhang, L. Aravind, Adenine methylation in eukaryotes: Apprehending the complex evolutionary history and functional potential of an epigenetic modification. *Bioessays* **38**, 27–40 (2016).
23. J. Chen *et al.*, Structural basis for MTA1c-mediated DNA N^6-adenine methylation. *Nat. Commun.* **13**, 3257 (2022).
24. M. Yue *et al.*, Coronaviral ORF6 protein mediates inter-organelle contacts and modulates host cell lipid flux for virus production. *EMBO J.* **42**, 23 (2023).
25. A. H. Hutagalung, P. J. Novick, Role of Rab GTPases in membrane traffic and cell physiology. *Physiol. Rev.* **91**, 119–149 (2011).
26. J. A. Eisen *et al.*, Macronuclear genome sequence of the ciliate *Tetrahymena thermophila*, a model eukaryote. *PLoS Biol.* **4**, e286 (2006).
27. T. Cheng *et al.*, Identification and characterization of the *de novo* methyltransferases for eukaryotic N^6-methyladenine (6mA). bioRxiv [Preprint] (2024). https://doi.org/10.1101/2024.03.25.586193 (Accessed 25 March 2024).
28. L. Lyu *et al.*, From germline genome to highly fragmented somatic genome: Genome-wide DNA rearrangement during the sexual process in ciliated protists. *Mar. Life Sci. Technol.* **6**, 31–49 (2024).
29. S. Urig *et al.*, The *Escherichia coli* dam DNA methyltransferase modifies DNA in a highly processive reaction. *J. Mol. Biol.* **319**, 1085–1096 (2002).
30. B. D. Giaimo, F. Ferrante, A. Herchenröther, S. B. Hake, T. Borggrefe, The histone variant H2A.Z in gene regulation. *Epigenetics Chromatin* **12**, 37 (2019).
31. S. Park, G. W. Kim, S. H. Kwon, J. S. Lee, Broad domains of histone H_3 lysine 4 trimethylation in transcriptional regulation and disease. *FEBS J.* **287**, 2891–2902 (2020).
32. B. D. Strahl, R. Ohba, R. G. Cook, C. D. Allis, Methylation of histone H_3 at lysine 4 is highly conserved and correlates with transcriptionally active nuclei in *Tetrahymena*. *Proc. Natl. Acad. Sci. U.S.A.* **96**, 14967–14972 (1999).
33. C. D. Allis *et al.*, hv1 is an evolutionarily conserved H2A variant that is preferentially associated with active genes. *J. Biol. Chem.* **261**, 1941–1948 (1986).
34. L. Duan *et al.*, Self-regulation of the DNA N_6-adenine methyltransferase AMT1 in the unicellular eukaryote *Tetrahymena thermophila*. bioRxiv [Preprint] (2024). https://doi.org/10.1101/2024.02.06.579081 (Accessed 26 February 2024).
35. X. Liu, B. Li, M. A. Gorovsky, Essential and nonessential histone H2A variants in *Tetrahymena thermophila*. *Mol. Cell. Biol.* **16**, 4305–4311 (1996).
36. B. Schuettengruber, A. M. Martinez, N. Iovino, G. Cavalli, Trithorax group proteins: Switching genes on and keeping them active. *Nat. Rev. Mol. Cell Biol.* **12**, 799–814 (2011).
37. A. Saettone *et al.*, The bromodomain-containing protein Ibd1 links multiple chromatin-related protein complexes to highly expressed genes in *Tetrahymena thermophila*. *Epigenetics Chromatin* **11**, 10 (2018).
38. Y. Taniguchi, The bromodomain and extra-terminal domain (BET) family: Functional anatomy of BET paralogous proteins. *Int. J. Mol. Sci.* **17**, 1849 (2016).
39. T. Fujisawa, P. Filippakopoulos, Functions of bromodomain-containing proteins and their roles in homeostasis and cancer. *Nat. Rev. Mol. Cell Biol.* **18**, 246–262 (2017).
40. S. Jha, A. Dutta, RVB1/RVB2: Running rings around molecular biology. *Mol. Cell* **34**, 521–533 (2009).
41. J. Wang, S. Gao, X. Peng, K. Wu, S. Yang, Roles of the INO80 and SWR1 chromatin remodeling complexes in plants. *Int. J. Mol. Sci.* **20**, 4591 (2019).
42. J. A. Downs *et al.*, Binding of chromatin-modifying activities to phosphorylated histone H2A at DNA damage sites. *Mol. Cell* **16**, 979–990 (2004).
43. A. Tosi *et al.*, Structure and subunit topology of the INO80 chromatin remodeler and its nucleosome complex. *Cell* **154**, 1207–1215 (2013).
44. C. Y. Zhou *et al.*, The yeast INO80 complex operates as a tunable DNA length-sensitive switch to regulate nucleosome sliding. *Mol. Cell* **69**, 677–688 (2018).
45. E. Oberbeckmann *et al.*, Genome information processing by the INO80 chromatin remodeler positions nucleosomes. *Nat. Commun.* **12**, 3231 (2021).
46. M. Zuber, E. M. Tan, M. Ryoji, Involvement of proliferating cell nuclear antigen (cyclin) in DNA replication in living cells. *Mol. Cell Biol.* **19**, 57–66 (1989).
47. F. Zölzer, O. Basu, P. U. Devi, S. P. Mohanty, C. Streffer, Chromatin-bound PCNA as S-phase marker in mononuclear blood cells of patients with acute lymphoblastic leukaemia or multiple myeloma. *Cell Prolif.* **43**, 579–583 (2010).
48. M. S. Kang *et al.*, Regulation of PCNA cycling on replicating DNA by RFC and RFC-like complexes. *Nat. Commun.* **10**, 2420 (2019).
49. B. Guillemette *et al.*, Variant histone H2A.Z is globally localized to the promoters of inactive yeast genes and regulates nucleosome positioning. *PLoS Biol.* **3**, e384 (2005).
50. C. Y. Okitsu, J. C. F. Hsieh, C. L. Hsieh, Transcriptional activity affects the H3K4me3 level and distribution in the coding region. *Mol. Cell. Biol.* **30**, 2933–2946 (2010).
51. S. Wahab, A. Saettone, S. Nabeel-Shah, N. Dannah, J. Fillingham, Exploring the histone acetylation cycle in the protozoan model *Tetrahymena thermophila*. *Front. Cell Dev. Biol.* **8**, 509 (2020).
52. Z. Wang *et al.*, Combinatorial patterns of histone acetylations and methylations in the human genome. *Nat. Genet.* **40**, 897–904 (2008).
53. L. G. Chicoine, C. D. Allis, Regulation of histone acetylation during macronuclear differentiation in *Tetrahymena*: Evidence for control at the level of acetylation and deacetylation. *Dev. Biol.* **116**, 477–485 (1986).
54. H. Hao *et al.*, RebL1 is required for macronuclear structure stability and gametogenesis in *Tetrahymena thermophila*. *Mar. Life Sci. Technol.* **6**, 183–197 (2024).
55. T. Jimenji, R. Matsumura, S. Kori, K. Arita, Structure of PCNA in complex with DNMT1 PIP box reveals the basis for the molecular mechanism of the interaction. *Biochem. Biophys. Res. Commun.* **516**, 578–583 (2019).
56. I. K. Mandemaker, W. Vermeulen, J. A. Marteijn, Gearing up chromatin: A role for chromatin remodeling during the transcriptional restart upon DNA damage. *Nucleus* **5**, 203–210 (2014).
57. V. A. Blomen, J. Boonstra, Stable transmission of reversible modifications: Maintenance of epigenetic information through the cell cycle. *Cell Mol. Life Sci.* **68**, 27–44 (2011).
58. K. R. Stewart-Morgan, N. Reverón-Gómez, A. Groth, Transcription restart establishes chromatin accessibility after DNA replication. *Mol. Cell* **75**, 284–297 (2019).
59. D. Tang *et al.*, Invasion by exogenous RNA: Cellular defense strategies and implications for RNA inference. *Mar. Life Sci. Technol.* **5**, 573–584 (2023).
60. X. Chen *et al.*, Enzymatic and chemical mapping of nucleosome distribution in purified micro-and macronuclei of the ciliated model organism, *Tetrahymena thermophila*. *Sci. China Life Sci.* **59**, 909–919 (2016).
61. F. Ye *et al.*, Comprehensive genome annotation of the model ciliate *Tetrahymena thermophila* by in-depth epigenetic and transcriptomic profiling. *Nucleic Acids Res.*, gkae1177 (2024). https://doi.org/10.1093/nar/gkae1177.
62. Y. Sheng *et al.*, The completed macronuclear genome of a model ciliate *Tetrahymena thermophila* and its application in genome scrambling and copy number analyses. *Sci. China Life Sci.* **63**, 1534–1542 (2020).